CXCR4 signaling determines the fate of hematopoietic multipotent progenitors by stimulating mTOR activity and mitochondrial metabolism

Vincent Rondeau, Maria Kalogeraki, Lilian Roland, Zeina Abou Nader, Vanessa Gourhand, Amélie Bonaud, Julia Lemos, Mélanie Khamyath, Clémentine Moulin, Bérénice Schell, et al.

CXCR4 signaling determines the fate of hematopoietic multipotent progenitors by stimulating mTOR activity and mitochondrial metabolism

Vincent Rondeau[1,2], Maria Kalogeraki[1,2], Lilian Roland[1,2,#], Zeina Abou Nader[1,2,#], Vanessa Gourhand[1,2], Amélie Bonaud[1,2], Julia Lemos[1,2], Mélanie Khamyath[1,2], Clémentine Moulin[1,2], Bérénice Schell[1,2], Marc Delord[3], Ghislain Bidaut[4], Séverine Lecourt[5], Christelle Freitas[1,2], Adrienne Anginot[1,2], Nathalie Mazure[6], David H. McDermott[7], Véronique Parietti[8], Niclas Setterblad[8], Nicolas Dulphy[1,2], Françoise Bachelerie[9], Michel Aurrand-Lions[2,4], Daniel Stockholm[10,11], Camille Lobry[12], Philip M. Murphy[7], Marion Espéli[1,2], Stéphane J.C. Mancini[13], and Karl Balabanian[1,2,*]

[1]Université Paris Cité, Institut de Recherche Saint-Louis, INSERM U1160, Paris, France.
[2]OPALE Carnot Institute, The Organization for Partnerships in Leukemia, Hôpital Saint-Louis, Paris, France.
[3]Direction à la recherche clinique et à l'innovation, Centre hospitalier de Versailles, Le Chesnay, France.
[4]Aix-Marseille Univ, CNRS, INSERM, Institut Paoli-Calmettes, CRCM, Marseille, France.
[5]Inserm U1279, Gustave Roussy Cancer Center, Université Paris Saclay, Villejuif, France.
[6]Centre Méditerranéen de Médecine Moléculaire, INSERM U1065, Nice, France.
[7]Molecular Signaling Section, Laboratory of Molecular Immunology, National Institute of Allergy and Infectious Diseases, NIH, Bethesda, MD, United States.
[8]Université Paris Cité, UMS Saint-Louis INSERM U53/UAR2030, Paris, France.
[9]Université Paris-Saclay, INSERM, Inflammation, Microbiome and Immunosurveillance, Orsay, France.
[10]PSL Research University, EPHE, Paris, France.
[11]Sorbonne Université, INSERM, Centre de Recherche Saint-Antoine, CRSA, Paris, France.
[12]Université Paris Cité, Institut de Recherche Saint-Louis, INSERM U944, Paris, France.
[13]Univ Rennes, INSERM, EFS, UMR S1236, Rennes, France.
[#]LR and ZAN: these authors contributed equally.
*Corresponding author. Email: karl.balabanian@inserm.fr

ABSTRACT

Both cell-intrinsic and niche-derived, cell-extrinsic cues drive the specification of hematopoietic multipotent progenitors (MPPs) in the bone marrow, which comprise multipotent MPP1 cells and lineage-restricted MPP2, MPP3, and MPP4 subsets. Patients with WHIM syndrome, a rare congenital immunodeficiency caused by mutations that prevent desensitization of the chemokine receptor CXCR4, have an excess of myeloid cells in the bone marrow. have an excess of myeloid cells in the bone marrow. Here, we investigated the effects of increased CXCR4 signaling on the localization and fate of MPPs. Knock-in mice bearing a WHIM syndrome–associated *CXCR4* mutation (*CXCR4*^{1013}) phenocopied the myeloid skewing of bone marrow in patients. Whereas MPP4 cells in wild-type mice differentiated into lymphoid cells, MPP4s in *CXCR4*^{1013} knock-in mice differentiated into myeloid cells. This myeloid rewiring of MPP4s in *CXCR4*^{1013} knock-in mice was associated with enhanced signaling mediated by the kinase mTOR and increased oxidative phosphorylation (OXPHOS). MPP4s also localized further from arterioles in the bone marrow of knock-in mice compared to wild-type mice, suggesting that the loss of extrinsic cues from the perivascular niche may also contribute to their myeloid skewing. Chronic treatment with the CXCR4 antagonist AMD3100 or the mTOR inhibitor rapamycin restored the lymphoid potential of MPP4s in knock-in mice. Thus, CXCR4 desensitization drives the lymphoid potential of MPP4 cells by dampening the mTOR-dependent metabolic changes that promote myeloid differentiation.

INTRODUCTION

Blood production is a tightly regulated process that starts with hematopoietic stem and progenitor cells (HSPCs). In adults, HSPCs are unique in their capacity to self-renew and replenish the entire blood system through production of a series of increasingly committed progenitor cells within the bone marrow (BM) microenvironment (1, 2). It is now well-established that HSPCs adapt the production of myeloid and lymphoid cells depending on the needs of the body (3). In mice, $CD34^-$ long-term (LT)-HSCs form a rare, quiescent population that displays a metabolism skewed towards anaerobic glycolysis at the expense of mitochondrial oxidative phosphorylation (OXPHOS) to preserve its quiescent state and long-term reconstitution capacity (4, 5). LT-HSCs differentiate first into $CD34^+$ short-term (ST)-HSCs that are characterized by shorter reconstitution ability (6) and then into hematopoietic multipotent progenitors (MPPs), which constitute the stage at which the major divergence of lymphoid and myeloid lineages occurs (7, 8). The MPP compartment can be divided into at least four subsets with different lineage fates (9-11). MPP1 share behaviors exhibited by ST-HSCs including multiple-lineage reconstitution ability (12). By contrast, megakaryocyte/erythroid (ME)-biased MPP2, granulocyte/macrophage (GM)-biased MPP3 and lymphoid-biased MPP4 subsets are more proliferative, devoid of self-renewal potential and likely rely less on glycolysis and more on OXPHOS for their metabolism as suggested by transcriptomic analysis (9, 12). The MPP compartment is also dynamic and functionally plastic. Under regenerative conditions, lymphoid-primed MPP4 contribute with their intrinsic GM poising to myeloid output at steady state and undergo a transient change in their molecular identity. This rewires them away from lymphoid differentiation to participate, together with overproduced MPP2 and MPP3, in the burst of myeloid production (10). During ageing, increased rate of myeloid cell production relies on higher number of myeloid-producing HSPCs. The MPP compartment appears to be pivotal in such age-related process

because ageing was associated with transcriptomic changes occurring primarily in MPPs, rather than in HSCs, and with a contraction of MPP4 within the BM (13).

The ability of MPPs to express both lymphoid and myeloid specific gene signatures is believed to confer to these cells a capacity to rapidly rewire their differentiation. MPP specification relies on the activity of specific transcription factors (TFs), which coordinate the expression of pro-lymphoid and pro-myeloid genes (10, 14-16). Ito-Nakadai *et al*. reported that the transcription factors Bach2 and C/EBPβ exert opposite effects in MPPs on the expression of target genes, with myeloid genes being activated by C/EBPβ and repressed by Bach2 while Bach2 simultaneously promotes expression of lymphoid genes (15). The deletion of *Ebf1*, which encodes the TF COE1, in all hematopoietic cells has been reported to exacerbate the myeloid potential of MPP3 and MPP4 by enhancing a myeloid signature of chromatin accessibility, overexpressing the myeloid TF C/EBPβα in MPP3 and increasing the capacity of MPP3 and MPP4 cells to generate $CD11b^{+}$ myeloid cells in vitro (16). These examples illustrate how the activities of different TFs tune MPP commitment into myeloid or lymphoid lineages.

Metabolic plasticity has emerged as a critical driver of HSC fate decision (17-19). The metabolite profiles of HSCs and MPPs are similar but differ from restricted progenitor populations and whole BM cells as shown by metabolomics analyses (20, 21). HSCs and MPPs share low amounts of glucose uptake, but MPPs display higher mitochondrial volume and membrane potential (22, 23). Metabolomics analyses revealed an enrichment in TCA cycle–related metabolites and amino acids in pooled MPP3 and MPP4 (MPP3/4) cells, whereas retinoic acid and one of its metabolites were enriched in HSCs including MPP1 (24). Because retinoic acid appears to play an essential role in maintaining quiescence and the self-renewal capacity of HSCs by instructing epigenetic and transcriptional landscapes, it seems likely that metabolic pathways may also play a role in shaping the cellular identity of MPPs.

HSPCs are thought to reside in perivascular niches that regulate their lifelong maintenance and differentiation (25). Perisinusoidal stromal cells promote HSC maintenance and retention in the BM notably by secreting niche factors such as stem cell factor (SCF) and the chemokine CXCL12 (26-28). MPPs subsets may also display distinct localization and stromal niches within BM (29, 30). It is also possible that regional BM localization of MPP subpopulations impacts their lineage specification and commitment. Although interleukin-1 (IL-1), IL-6, and tumor necrosis factor (TNF) have been proposed to reprogram MPP4 (31-33), our understanding of how cell-extrinsic niche-related and cell-intrinsic cues drive the lymphoid versus myeloid fate decision of MPPs is still fragmentary. Kang *et al*. reported molecular and functional heterogeneity among MPP3 by identifying a subset of MPP3 that serves as a reservoir for rapid production of myeloid cells in stress and disease conditions (29). This occurs through intrinsic lineage-priming toward myeloid differentiation and cytokine production in the BM. Signaling by the G protein–coupled receptor CXCR4 on MPPs in response to CXCL12 produced by BM perivascular stromal cells constitutes a key pathway through which the niche and MPPs communicate. Deletion of *Cxcr4* in total MPPs reduced their differentiation into common lymphoid progenitors (CLPs) and decreased lymphopoiesis (34) but also imbalanced HSC homeostasis as well as access to niche factors such as membrane SCF (35). Using a lymphopenic mouse model bearing a gain-of-function mutation of *Cxcr4* described in the rare human immuno-hematological disorder warts, hypogammaglobulinemia, infections, myelokathexis (WHIM) syndrome (WS) (36), we reported that Cxcr4 signaling termination, also called desensitization, is required for quiescence and cell cycling balance of murine HSCs and their differentiation into multipotent and downstream lymphoid-biased progenitors (37). These studies did not address the heterogeneity of lineage-biased MPPs or the molecular mechanisms that promote MPP fate in a Cxcr4-driven manner. Here, we interrogated the mechanisms driving lymphoid-myeloid fate

of MPPs by analyzing subsets of MPPs that were wild-type (WT) or carried the gain-of-function *Cxcr4* mutation (*Cxcr4*^{1013}). We found that proper Cxcr4 signaling was required for MPP4 to maintain their lymphoid potential, prevent overactive metabolism, and allow their positioning near peri-arteriolar structures, thereby likely regulating their access to external cues.

RESULTS

The HSPC compartment is myeloid-skewed in the BM of WS mice and patients

To determine whether impaired Cxcr4 desensitization impacted MPP heterogeneity in the BM, a multi-parametric flow cytometry-based strategy was used on the marrow fraction (obtained by centrifugation of the diaphysis) from adult *Cxcr4*$^{+/+}$ (WT) and *Cxcr4*^{1013} knockin heterozygous (+/1013) and homozygous (1013/1013) mice as previously reported (9-12). Mutant mice were generated by a knockin strategy to bear a common mutation reported in WS patients at nucleotide 1013, the *CXCR4*^{1013} mutation (36). This mutation introduces a stop codon to replace Ser^{338} in the C-tail of CXCR4, deleting the terminal 15 amino acids and preventing efficient desensitization of the receptor as well as internalization upon activation. MPPs are found in the Lin$^-$/Sca-1$^+$/c-Kit$^+$ (LSK) fraction and the amounts of CD34, CD48, CD150 and Flt3/CD135 markers divide the MPP pool into MPP1 or ST-HSCs (CD34$^+$Flt3$^-$CD150$^+$CD48$^-$), myeloid-biased MPP2 (CD34$^+$Flt3$^-$CD150$^+$CD48$^+$) and MPP3 (CD34$^+$Flt3$^-$CD150$^-$CD48$^+$) subsets, and the lymphoid-biased MPP4 (CD34$^+$Flt3$^+$CD150$^-$CD48$^{-/+}$) subpopulation (Fig. 1A) (10). First, we assessed the ex vivo expression of the signaling trio formed by Cxcl12 and its two receptors Cxcr4 and Ackr3 within MPP subsets. Surface expression of Cxcr4 was similarly detected in WT and knockin MPP subsets as determined by flow-cytometric analyses (Fig. 1B and fig. S1A). Expression of Ackr3 was also observed on the surface of WT and knockin MPPs but was lower than in Lin$^+$ cells (fig. S1B). The absence

of Cxcl12 expression in MPPs was established using *Cxcl12*^{Dsred} reporter mice (fig. S1C). As expected, +/1013 and 1013/1013 MPPs displayed impaired Cxcr4 internalization following Cxcl12 stimulation as well as increased Cxcl12-promoted chemotaxis in a manner that depended on the *Cxcr4*^{1013} allele, which was abolished by the specific Cxcr4 antagonist AMD3100 (Fig. 1C and fig. S1D). These dysfunctions were not secondary to modulation of membrane Cxcr4 expression but likely relied on the enhanced signaling properties of the truncated Cxcr4 receptor upon Cxcl12 binding, as revealed by Akt PhosphoFlow analyses (Fig. 1D). Thus, the desensitization-resistant C-tail–truncated Cxcr4^{1013} receptor is expressed and has increased signaling properties in all MPP subsets.

We next compared the BM composition of WT and knockin mice with regards to MPP subsets. We observed a reduction of the proportion and number of MPP4 in a *Cxcr4*^{1013} allele dose-dependent pattern (Fig. 1, A and E). This was mirrored by an increase in the MPP2 and MPP3 (MPP2/3) subsets, thus suggesting that the MPP compartment in *Cxcr4*^{1013} knockin mice is myeloid-biased and defective for lymphoid potential. As previously reported (36, 37), knockin mice had normal numbers of LT-HSCs, MPP1/ST-HSCs, common myeloid progenitors (CMPs), granulocyte-monocyte progenitors (GMPs), and megakaryocyte-erythroid progenitors (MEPs) and decreased numbers of CLPs in BM, and displayed circulating lympho-neutropenia compared with WT mice (fig. S1, E and F). Knockin mice also exhibited preserved numbers of MPP5 and MPP6, two subsets positioned upstream of MPP2-4 within the hematopoietic tree (11) (fig. S1E). Although lineage-biased MPP subsets are not described in the classical human hematopoietic differentiation tree (38, 39), a similar pro-myeloid skewing was observed in BM samples from two unrelated patients with WS, both of whom are heterozygous for the autosomal-dominant *CXCR4*^{R334X} mutation (Fig. 1, F to H and fig. S1G). Frequencies and numbers of CD34^{+} HSPCs and lymphoid-committed progenitors including immature multi-lymphoid progenitors (MLPs; defined as

CD45RA^{+}CD38^{-}CD7^{-}CD34^{+}CD10^{+}) and their progeny CLPs (defined as CD45RA^{+}CD38^{+}CD34^{+}CD10^{+}) tended to decline in the BM of WS patients compared with aged- and sex-matched healthy individuals. Conversely, the frequencies of CMPs (defined as CD45RA^{-}CD38^{+}CD7^{-}CD34^{+}CD10^{-}CD135^{+}) and downstream GMPs (defined as CD45RA^{+}CD38^{+}CD7^{-}CD34^{+}CD10^{-}CD135^{+}) tended to increase, whereas their numbers were similar to those observed in healthy individuals. Surface expression of CXCR4 was comparable in healthy and WS HSPCs (Fig. 1I). Thus, these findings unravel a myeloid skewing of the HSPC compartment in the BM of WS mice and patients.

CXCR4 desensitization is required for efficient generation and maintenance of the lymphoid-biased MPP4 pool

At steady state, MPP subsets are independently produced by ST-HSCs or MPP1 that give rise to higher number of MPP4 than of MPP2 and MPP3 (10). Thus, we hypothesized that the overall myeloid skewing of the knockin MPP compartment could involve an impaired differentiation potential of MPP1. We compared in vitro the capacity of MPP1 sorted from the BM of WT or knockin mice to generate biased MPP subsets in feeder-free media (37). By day 4, the number and proportion of MPP4 were significantly lower in *Cxcr4*^{1013} knockin cell cultures compared with the WT ones (Fig. 2A). In contrast, knockin MPP1 were as efficient as WT ones at producing MPP2/3. Addition of the CXCR4 antagonist AMD3100 rescued the lymphoid potential of knockin MPP1 because it led to increased frequency and number of MPP4, reaching the ones observed in WT cultures (Fig. 2A). Therefore, knockin MPP1 display impaired capacity to differentiate into MPP4 but not into myeloid-biased MPPs and this likely relies on aberrant Cxcr4 signaling.

Epigenetic mechanisms including chromatin accessibility dynamics have been reported to regulate the fate of HSPCs (19, 40). Thus, we interrogated if impaired

differentiation capacity of knockin MPP1 was associated with dysregulations in chromatin accessibility by performing assay for transposase-accessible chromatin sequencing (ATAC-seq). In 1013/1013 MPP1, we identified 628 increased and 612 reduced ATAC-seq peaks compared to WT MPP1 (Fig. 2B, fig. S2A and data file S1). Gene ontology (GO) analyses on regions associated with decreased chromatin accessibility revealed an enrichment for lymphoid differentiation signatures (Fig. 2B and data file S2). Conversely, these analyses on regions associated with increased chromatin accessibility revealed an enrichment for several myeloid differentiation signatures including "regulation of myeloid cell differentiation" (GO: 0045637), "granulocyte differentiation" (GO: 0030851) and "myeloid cell differentiation" (GO: 0030099), although these GO terms were not among the Top100 most enriched (fig. S2A and data file S3). To determine whether reduced and increased ATAC-seq peaks harbor TF binding motifs relevant for lymphoid-myeloid differentiation, we then performed TF motif enrichment analysis using HOMER. In regions associated with decreased chromatin accessibility, we found within the top 5 highest enriched motifs Fli1, ERG and GABPA TF motifs (Fig. 2C and data file S4). Of note, such TF are known to be important regulators of lymphoid differentiation (41-43). Increased ATAC-seq peaks were enriched for different motifs previously reported to be enriched in myeloid- and megakaryocyte-biased HSCs such as PU.1, Ets1 and Runx1 (44, 45) (data file S5). These data prompted us to evaluate in vitro the ability of WT or knockin MPP1 to generate mature lymphoid cells. When cultured on OP9/IL-7 stromal cells, knockin MPP1 gave rise to approximately 3-times fewer B cells (defined as $B220^{+}CD11b^{-}$) compared to WT ones and this was rescued by AMD3100 notably in 1013/1013 cultures (Fig. 2D). Additionally, we assessed using this co-culture system the lymphoid potential of MPP3 and MPP4 generated in vitro from MPP1 in feeder-free conditions. As expected, MPP4 sorted from WT MPP1 cultures were more poised to generate B cells than MPP3, indicating that the specific lymphoid skewing of MPP4 was still apparent

after feeder-free culture conditions (Fig. 2E). However, knockin MPP4 displayed an impaired capacity to produce B cells, particularly in 1013/1013 cultures, suggesting that Cxcr4-mediated epigenetic changes established at the MPP1 level might be inherited by MPP4 upon differentiation, leading to reduced lymphoid potential at the MPP4 stage. In line with this, we observed by ATAC-seq in 1013/1013 MPP4 an enrichment for lymphoid differentiation signatures in regions associated with decreased chromatin accessibility (Fig. 2F and data file S6). In total, we detected 273 increased and 419 reduced ATAC-seq peaks in 1013/1013 MPP4 compared to WT MPP4 (Fig. 2F, fig. S2B and data file S7). GO analyses on increased ATAC-seq peaks in knockin MPP4 did not unveil myeloid differentiation signatures (data file S8). In 1013/1013 MPP4, we found that Fli1 and ERG were among the top 5 highest enriched motifs in reduced ATAC-seq peaks, whereas PU.1 was among the top 5 highest enriched motifs in increased ATAC-seq peaks (Fig. 2G and data files S9 and S10) as already observed at the MPP1 stage (Fig. 2C and data files S4 and S5). Collectively, these findings identify a reduction of lymphoid potential at the MPP1 stage in *Cxcr4*^{1013} knockin mice that occurs at the molecular and functional levels and is transmitted to the MPP4 stage upon differentiation.

We then investigated by flow cytometry the impact of the *Cxcr4* mutation on both the survival and proliferative capacities of MPPs. Abnormal Cxcr4 signaling was associated with decreased fractions of apoptotic cells (Annexin-V$^+$DAPI$^-$) in *Cxcr4*^{1013} knockin myeloid-biased MPP2/3, whereas no changes were observed in MPP4 (fig. S2C). With regards to the cycling status, a significant increase in the frequency of cells in the S/G2-M phases (DAPI$^+$Ki-67$^+$) was observed among knockin MPP3 and MPP4 subsets (Fig. 2H and fig. S2D). This was associated with reduced frequencies of cells in the G1 phase, thus indicating enhanced G1-S transition in *Cxcr4*^{1013} knockin MPP3 and MPP4. In contrast, the MPP2 pool was unchanged, whereas knockin MPP1 displayed increased quiescence as previously reported (37). This was confirmed by in vivo BrdU pulse-chase assays. After a 12-day pulse

period, we observed a *Cxcr4*^{1013} allele dose–dependent increase in BrdU incorporation within knockin MPP3 and MPP4 (fig. S2E). After 3 weeks of chase, higher proportions of *Cxcr4*^{1013} knockin MPPs had lost label-retaining cell activity compared with WT ones. Therefore, the quiescence/cycling balance and survival profile are differentially disturbed in knockin MPP subpopulations, and those dysregulations may contribute to the myeloid skewing by promoting the accumulation of MPP2/3. Paradoxically, increased cycling of knockin MPP4 is associated with contraction of this pool, which evokes aging-induced loss of MPP4 with altered cycling and lymphoid priming (46). Altogether, these results indicate that proper Cxcr4 desensitization is required for efficient generation and maintenance of the lymphoid-biased MPP4 pool.

CXCR4 desensitization is required for MPP4 positioning near BM perivascular structures

To determine whether changes in the MPP compartment of *Cxcr4*^{1013} knockin mice resulted from cell-intrinsic or -extrinsic defects, we performed short-term (3 weeks) and long-term(16 weeks) BM reconstitution experiments. First, BM cells from WT, +/1013, or 1013/1013 CD45.2^{+} mice were transplanted into lethally irradiated WT CD45.1^{+} recipients (Fig. 3A). Three or 16 weeks later, there were significantly lower numbers of MPP4 in the BM of *Cxcr4*^{1013} knockin BM-chimeric mice compared with WT chimeras (Fig. 3B). This was mirrored by a slight increase in MPP2/3 subsets. To rule out the possibility that alterations of the stromal compartment by the donor-derived hematopoietic cells contributed to these phenotypes, we then performed competitive BM transplantation experiments in which total marrow cells from CD45.2^{+} WT, +/1013, or 1013/1013 mice were co-injected with CD45.1^{+} WT total marrow cells into lethally irradiated CD45.1^{+}/CD45.2^{+} WT recipient mice (Fig. 3C). Chimerism in blood and BM were analyzed after 3 weeks of reconstitution. As previously

reported (47-48), our results showed a competitive suppression of +/1013 $CD19^+$ and $CD11b^+$ cell subset reconstitution in peripheral blood by WT hematopoiesis in the same mouse (fig. S3A). This competitive disadvantage was even more marked in competitive transplantation experiments between 1013/1013 and WT BM cells. Regarding hematopoietic reconstitution within BM, $Cxcr4^{1013}$ knockin marrow cells were as efficient as WT marrow cells at replenishing MPP2/3 subsets after competitive transplantation (Fig. 3D). By contrast, WT marrow cells were superior than $Cxcr4^{1013}$ knockin marrow cells for reconstituting MPP4 and CLPs. We also performed reverse chimeras in which $CD45.2^+$ WT and knockin mice were irradiated and reconstituted with WT $CD45.1^+$ BM (Fig. 3E). The numbers of MPP4 in the BM were comparable in all groups, whereas MPP2/3 were slightly increased in the BM of knockin mice (Fig. 3F). Together with in vitro differentiation findings (Fig. 2A), these results suggest that the contraction of the MPP4 population in the BM of $Cxcr4^{1013}$ knockin mice involves cell-intrinsic effects of impaired Cxcr4 desensitization, whereas the expansion of myeloid-biased MPPs may result from combinatorial effects of aberrant Cxcr4 signaling in both stromal (extrinsic signals) and hematopoietic (intrinsic signals) cells.

Although the loss of MPP4 in $Cxcr4^{1013}$ knockin mice appeared to arise from hematopoietic cell-intrinsic defects, the possibility that enhanced Cxcr4 signaling results in mislocalization of knockin MPP4 within the BM, and ultimately leads to suboptimal access to external cues required for their maintenance and/or fate, remained to be explored. The BM localization of MPP subsets and their supporting stromal niches are still incompletely defined (29, 30, 49). To evaluate the BM positioning of MPP4, we combined in situ hybridization–based RNA-scope assay and immunofluorescence staining (Fig. 3G and fig. S3, B and C). In line with the contraction in knockin MPP4 observed by flow cytometry (Fig. 1, A and E), the frequency of c-$Kit^+Sca\text{-}1^+Flt3^+$ cells that are enriched for MPP4 was decreased in the BM of 1013/1013 mice (Fig. 3, G and H and fig. S3, B and C). No clustering of WT or knockin

MPP4 was observed within BM sections as determined using nearest neighbor index calculation (fig. S3D). We then investigated the positioning of WT and Cxcr4^{1013} knockin MPP4 relative to arteriolar cells defined as Laminin^{+}Sca-1^{+} (fig. S3E) (50, 51). Compared to WT mice, knockin mice displayed preserved proportions of arteriolar cells (fig. S3F) and the vast majority of arteriolar cells was found to express Cxcl12 independently of their *Cxcr4* mutational status (Fig. 3I, fig. S4). Strikingly, knockin MPP4 were localized at greater distances from arteriolar cells compared to WT MPP4 (Fig. 3J). Reduction of phosphorylated STAT5α has been associated with defective positioning of CLPs and pro-B cells near IL-7^{+} perivascular stromal cells (34, 52). This prompted us to assess STAT5α status in WT and knockin MPP4 ex vivo. Compared to WT MPP4, knockin MPP4 displayed decreased STAT5α phosphorylation in the absence or presence of Cxcl12 (Fig. 3K). Altogether, these findings are suggestive of an altered in situ distribution of MPP4 carrying the gain of function *Cxcr4* mutation within BM that could affect access to critical niche factors controlling their maintenance and fate.

CXCR4 desensitization is required to maintain the molecular identity of MPP4

We next investigated the impact of the gain of Cxcr4 function on the molecular identity of biased MPP subsets with a focus on MPP4. RNA-seq analyses of sorted bulk cells yielded robust and reproducible data for all samples with more than 8 x 10^7 reads per sample (Fig. 4A). In total, transcripts corresponding to 20,644 genes were identified. The different MPP subsets clustered distinctly in WT and knockin mice as shown by principal component analysis (PCA) (fig. S5A). We then applied the gene signatures reported by Pietras *et al*. (10) and representing the 50 most highly differentially expressed genes in each MPP subset to our RNA-seq data from WT mice. Gene set enrichment analyses (GSEA) revealed that MPP2-4 signatures were enriched in the corresponding MPP subset, thus validating the robustness of

our study (fig. S5B). Unsupervised analyses of RNA-seq data highlighted 73 genes that were differentially expressed between WT and +/1013 MPP4 compared to 717 genes between WT and 1013/1013 MPP4. Volcano plots of differentially regulated genes indicated that most of these were enriched in 1013/1013 MPP4 (Fig. 4B and data file S11). Only 56 and 77 genes were differentially expressed between WT and 1013/1013 MPP1 and between WT and 1013/1013 MPP3, respectively, and without any biological process significantly enriched (fig. S5, C and D), suggesting that MPP1 and MPP3 do not share similar requirements for the Cxcl12-Cxcr4 signaling axis to regulate their molecular identity compared to MPP4. We then performed GO analyses on genes showing increased or decreased expression in 1013/1013 MPP4 compared to WT ones to determine which biological processes were impacted in knockin MPP4. In line with our cell cycling analyses (Fig. 2H and fig. S2, D and E), the MPP4 signature in 1013/1013 mice was enriched for genes related to cell cycle progression and regulation (Fig. 4C and data file S12). Moreover, genes related to OXPHOS metabolism appeared to be overrepresented in knockin MPP4. In contrast, expression of key regulators of lymphoid differentiation were decreased in knockin MPP4 (Fig. 4C). Altogether, these results reveal an imbalance in the molecular identity of $Cxcr4^{1013}$ knockin MPP4.

CXCR4 signaling termination is required to maintain the lymphoid potential in MPP4

We next determined whether $Cxcr4^{1013}$ knockin MPP4 displayed an imbalance in the lymphoid-myeloid gene landscape. Heatmap analysis of RNAseq-based expression data for 48 genes comprised in the GO “Lymphoid differentiation” (GO:0030098) and expressed in WT MPP4 revealed differential expression gene profiles between WT and knockin MPP4 with a significant decrease of the lymphoid signature in 1013/1013 MPP4 (Fig. 5A). This was confirmed by microfluidic-based multiplex gene expression analyses on MPP4. WT and knockin MPP4 clustered differentially along relative expression of master regulators of

lymphoid and myeloid differentiation (Fig. 5B and table S1). There was significantly decreased expression of key lymphoid differentiation genes including *Ikzf1*, *Flt3*, and *Dntt* in knockin MPP4 that followed a *Cxcr4*^{1013} allele copy number–dependent pattern (Fig. 5C). This was associated with increased expression of pro-GM genes such as *Mpo* and *Irf8* (53, 54), whereas the expression of pro-ME genes such as *Gfi1b* (55) was preserved (Fig. 5D). Reductions in Flt3 protein and increases in Irf8 protein in knockin MPP4 were validated by flow cytometry (Fig. 5E). Collectively, these findings suggest a global skewing of the MPP compartment that promoted myeloid differentiation likely at the expense of the lymphoid lineage in knockin mice. The fate of the MPP4 subset would be pivotal in such a process.

To test this, we first assessed in vitro the B-cell differentiation potential of WT and Cxcr4^{1013} knockin MPP4. When cultured on OP9/IL-7 stromal cells, knockin MPP4 differentiation toward B cells was significantly decreased as compared to WT MPP4, and this was rescued by AMD3100 treatment (Fig. 5F). Second, we compared in vitro the capacity of MPP4 sorted from the marrow of WT or Cxcr4^{1013} knockin mice to generate committed myeloid or lymphoid progenitors and mature cells in feeder-free media. By day 4, both the frequencies and numbers of myeloid-committed progenitors, including GMPs (defined as LK CD16/32^{+}CD34^{+}), contained in the Lin^{-}Sca-1^{-}c-Kit^{+} (LK) fraction were significantly higher in Cxcr4^{1013} knockin cell cultures compared with WT ones (Fig. 5G). This likely accounted for the increase in mature myeloid cells expressing both Gr1 and CD11b markers in knockin cultures by day 7. In contrast, the proportions of Lin^{-}Sca-1^{low}c-Kit^{low} cells that comprise CLPs were reduced in knockin MPP4 cultures compared with the WT ones. Moreover, we were able to recover at day 4 significant proportions of Flt3^{low} cells from both WT and knockin MPP4 cultures, and this was amplified in the knockin cultures (Fig. 5H), thus suggesting that knockin MPP4 may undergo a molecular reprogramming that renders them functionally and phenotypically close to GM-biased MPP3. This likely relied on fine-tuned Cxcr4 signaling,

because addition of 10 μM AMD3100 at the start of the assay reduced the representation of $Flt3^{low}$ cells and restored the expression of Flt3 on knockin MPP4 (Fig. 5, H and I). To demonstrate the myeloid bias of $Cxcr4^{1013}$ knockin MPP4, we transplanted MPP4 isolated from the BM of WT or knockin $CD45.2^{+}$ mice into sub-lethally irradiated WT $CD45.1^{+}$ recipient mice and analyzed their multi-lineage output 14 days later (fig. S6A). As expected, WT MPP4 mostly (~80%) gave rise to lymphoid-derived progeny in the BM of recipient mice (Fig. 5J). In $Cxcr4^{1013}$ knockin MPP4-chimeric mice, the lymphoid output was reduced and this was mirrored by an increase in donor-derived myeloid cells. A similar increase in myeloid output was observed in the peripheral blood of $Cxcr4^{1013}$ knockin MPP4-chimeric mice (fig. S6B). Taken together, these findings unveil an imbalance in the lymphoid-myeloid gene landscape of $Cxcr4^{1013}$ knockin MPP4 that likely affects their capacity to produce lymphoid cells.

These results led us to investigate whether the Cxcl12-Cxcr4 signaling axis plays a role in regulating the fate of MPP4 under physiological conditions. To this end, sorted WT MPP4 were cultured in feeder-free medium in the presence or absence of Cxcl12 and AMD1300 and generation of GMPs and mature myeloid cells was assessed after four and seven days of culture, respectively. Addition of Cxcl12 promoted the differentiation of WT MPP4 into GMPs (day 4) and mature myeloid cells (day 7) and this was abolished by AMD3100 treatment (Fig. 5K), suggesting that the Cxcl12-Cxcr4 signaling axis regulates the fate of MPP4 under normal physiological conditions. These findings further indicated that in the context of increased Cxcr4 signaling, the pro-myeloid effect is exacerbated in $Cxcr4^{1013}$ knockin MPP4 and this rewiring might account for the BM accumulation of myeloid-biased MPPs in an additive manner with the imbalance in quiescence/cycling and survival profiles of MPP2/3 subsets.

Overactive OXPHOS-driven metabolism in Cxcr4^{1013} knockin MPP4

Metabolic pathways contribute to HSC self-renewal and fate restriction that rely on differential energy needs (4, 5, 17, 56). When HSCs differentiate, they exit from quiescence and undergo a metabolic switch from anaerobic glycolysis to mitochondrial OXPHOS. Transcriptional and metabolomics studies suggest that MPP subsets are more dependent on OXPHOS for their metabolism than are HSCs, as illustrated by enrichment in TCA cycle–related genes and metabolites compared to HSCs (12, 24). To address whether and how Cxcr4 signaling controls the metabolic profiles of MPP subsets, we performed GSEA enrichment and heatmap analysis of RNA-seq data. These revealed a significant enrichment in the expression of genes encoding OXPHOS components particularly in 1013/1013 MPP4, but also in +/1013 MPP4 (fig. S7A). No alteration of the glycolysis-related gene signature was observed between WT and knockin MPP4 (fig. S7B). Flow-cytometric examination of mTOR and downstream targets such as ribosomal protein S6 showed increased phosphorylation in knockin MPP4 in response to Cxcl12 (Fig. 6A), indicating a state of increased metabolic activity, including the mTOR pathway. These responses were sensitive to AMD3100 and not observed for the p38 mitogen-activated protein kinase (MAPK) pathway (fig. S7C), further suggesting that Cxcl12-promoted Cxcr4 signaling is relayed through the Akt-mTOR pathway in MPP4. In agreement with their overexpressed OXPHOS signature, Cxcr4^{1013} knockin MPP4 showed increased oxygen consumption rate (OCR), whereas extracellular acidification rate (ECAR) measurements were reduced compared to WT MPP4 as revealed by Seahorse analyses (Fig. 6B). OXPHOS metabolism is associated with the production of mitochondrial metabolites such as reactive oxygen species (ROS). Consistent with this, knockin MPP4 were poised to produce higher concentrations of ROS than were WT MPP4 as shown by MitoSox, CellRox, or DCFDA staining (fig. S7D). In contrast, knockin MPP4 displayed reduced glucose uptake rate compared to WT MPP4 as shown by 2-NBDG incorporation assay (fig.

S7E). Collectively, these results revealed an overactive OXPHOS-driven metabolism in Cxcr4^{1013} knockin MPP4.

We next interrogated if these metabolic dysregulations were associated with altered mass and activity of mitochondria where OXPHOS occurs. WT and knockin MPP4 exhibited similar mitochondrial mass as shown by MitoTrackerGreen (MTG) (19) or mitochondrial transcription factor A (TFAM) (57) staining (Fig. 6C and fig. S7F). By contrast, decreased contents of mitochondrial membrane potential dye tetramethylrhodamine-ethyl-esther (TMRE) were observed in Cxcr4^{1013} knockin MPP4 (Fig. 6C). TMRE is thought to accumulate specifically in active mitochondria and to decrease in damaged mitochondria, which are characterized by a loss of membrane potential (19, 58). In agreement, immunofluorescence staining for the translocase of the outer membrane of mitochondria 20 (TOMM20) were punctate in knockin MPP4 as compared to the hyperfused profile in WT ones (Fig. 6D), suggesting the presence of damaged mitochondria in Cxcr4^{1013} knockin MPP4. These findings prompted us to assess the effect of Cxcl12 signaling on the mitochondrial metabolic activity of MPP4 under physiological conditions. Treatment of sorted WT MPP4 for 24 hours with as low as 1 nM Cxcl12 led to reduced TOMM20 mean fluorescence intensity (MFI) as well as a decrease in the number of mitochondrial fragments per cell (Fig. 6E). Sorted WT MPP4 were cocultured with OP9/IL-7 stromal cells in the presence or absence of Cxcl12 and AMD3100 in order to evaluate the impact of the Cxcl12-Cxcr4 axis on the mitochondrial mass and membrane potential in steady state conditions. After 24 hours, we observed decreased MTG and TMRE contents in WT MPP4 following addition of Cxcl12, and this was reversed by AMD3100 treatment (Fig. 6F). Together, these findings suggest a role for the Cxcl12-Cxcr4 signaling axis in regulating mitochondrial metabolic activity of WT MPP4 at baseline. Moreover, knockin MPP1 also displayed enhanced mTOR signaling and decreased TMRE content (fig. S7, G to I). Therefore, these

findings suggest a deteriorated mitochondrial activity in knockin MPP4 that display hyper-proliferative and myeloid-biased status.

To further determine whether the remodeling of mitochondrial machinery in knockin MPP4 was associated with skewing to the myeloid lineage, we sought to segregate the MPP4 subset in two fractions depending on TMRE expression, positive/high (Fraction A) vs negative/low (Fraction B), enriched in WT and knockin MPP4 respectively (Fig. 6G). Both MPP4 fractions were sorted and characterized for differentiation capacities. In vitro feeder-free differentiation assays showed that fraction B from WT MPP4 was more poised to give rise to GMPs and mature myeloid cells than was fraction A, and this was enhanced with knockin MPP4 (Fig. 6H). These data suggested that increased myeloid output of $Cxcr4^{1013}$ knockin MPP4 cultures (Fig. 5G) was likely due to over-representation of the myeloid-biased fraction B at the start of the assay. In agreement, expression of key pro-GM genes such as *Mpo* and *Irf8* were increased in fraction B of knockin mice, as shown by microfluidic-based qPCR from $TMRE^{low}$ MPP4 at the single-cell level (Fig. 6I). Congruent with our in vitro differentiation findings (Fig. 6H), WT $TMRE^{low}$ (fraction B) MPP4 were more poised than WT $TMRE^{high}$ (fraction A) MPP4 to give rise to myeloid cells upon transplantation into sub-lethally irradiated WT $CD45.1^{+}$ recipient mice (Fig. 6J). This myeloid output was increased in the BM of 1013/1013 fraction B MPP4-chimeric mice compared to mice transplanted with WT fraction B MPP4. This was mirrored by a decrease in the lymphoid output in the BM of knockin MPP4-chimeric mice.

Finally, we studied the impact of modulating specific metabolic pathways on MPP4 fate. Treatment with mitochondria-targeted antioxidant Mitoquinol (Mito-q) or uncoupling agent for OXPHOS carbonyl cyanide m-chlorophenyl hydrazone (CCCP) led to decreased numbers of mature myeloid cells in WT and knockin MPP4 cultures without affecting cell viability (Fig. 6K and fig. S7J). In contrast, addition of N-acetyl-L-cysteine (NAC) had no

impact on MPP4 differentiation, suggesting a minor role of ROS in regulating such a process (fig. S7, K and L). Altogether, these results suggest that accumulation of damaged mitochondria and overactive OXPHOS-driven metabolism are associated with myeloid-biased differentiation of MPP4 in absence of Cxcr4 desensitization.

Modulation of the Cxcr4-mTOR signaling axis normalizes the fate properties of Cxcr4^{1013} knockin MPP4

The above findings led us to determine whether targeting the Cxcl12-Cxcr4 signaling axis or the mTOR pathway would counteract myeloid skewing of knockin MPP4. First, we evaluated in vitro the impact of AMD3100 on the myeloid potential of TMRE^{low} MPP4. We treated TMRE^{low} MPP4 with 10 µM AMD3100, a dose sufficient to normalize Cxcr4 signaling in knockin cells (Fig. 6A). Inhibition of Cxcr4 signaling led to a decreased myeloid output by days 4 and 7 from both WT and knockin TMRE^{low} MPP4 cultures (Fig. 7A). This occurred without affecting cell viability and by promoting the accumulation of TMRE^{low} MPP4, suggesting a blockage of MPP4 differentiation (fig. S8, A and B). Such a treatment was even sufficient to normalize at day 7 the production of mature myeloid cells from 1013/1013 TMRE^{low} MPP4 cultures, thus supporting a role for Cxcr4 signaling in regulating the myeloid program of MPP4 with altered mitochondrial activity. Similar results were obtained with doses as low as 10 nM AMD3100 (fig. S8C), thus ruling out the possibility of off-target effects or non-neutral activity of AMD3100 on Cxcr4. We also assessed the impact of daily intraperitoneal injections for 3 weeks of 5 mg/kg AMD3100 (59, 60) on the BM composition of WT and knockin mice with regards to HSPCs and mature lymphoid and myeloid cells (Fig. 7B). Cxcr4 inhibition decreased the number of MPP4 in the BM of WT mice (Fig. 7C). In knockin mice, AMD3100 treatment reversed the quantitative defect in MPP4 (Fig. 7C) and CLPs (defined as Lin$^-$Sca-1^{low}c-Kit^{low} Flt3$^+$CD127$^+$) (fig. S8D) with absolute numbers

reaching those observed in untreated WT mice. Such a treatment also led to a slight expansion of the MPP1 subset but had no significant effect on LT-HSC, MPP2, or MPP3 numbers in 1013/1013 mice (fig. S8D). Chronic blockade of Cxcr4-dependent signaling in knockin mice corrected the number of mature B cells within the BM as well as the circulating lymphopenia (Fig. 7D and fig. S8E). By contrast, such a treatment had no impact on CMPs (defined as LK CD16/32^{-}CD34^{+}), GMPs, MEPs (defined as LK CD16/32^{-}CD34^{-}), or mature myeloid cells representation (fig. S8, D and E). This led us to analyze to what extent AMD3100 treatment impacted the mitochondrial activity of the MPP4 subset. After 3 weeks of treatment, we observed that TMRE contents in knockin MPP4 increased to become similar to WT MPP4 (Fig. 7E). This was due to normalization of the fraction B. Therefore, these data suggest that the integrity of Cxcl12-Cxcr4 signaling is required for maintaining the MPP4 subset and its mitochondrial metabolic activity.

Finally, we tested the possibility that Cxcr4 signaling regulates metabolic and fate properties of MPP4 through the sensor mTOR. Upon Cxcl12 stimulation in vitro, knockin TMRE^{low} MPP4 displayed higher phosphorylated mTOR content than WT TMRE^{low} MPP4, and this was abolished by AMD3100 treatment (Fig. 7F). These findings prompted us to evaluate in vitro the impact of the mTOR inhibitor rapamycin at 250 nM on the myeloid potential of TMRE^{low} MPP4. This resulted in accumulation of TMRE^{low} MPP4 and decreased numbers of GMPs and mature myeloid cells from both WT and knockin cultures (Fig. 7A and fig. S8, A and B), suggesting the involvement of mTOR signaling in the fate properties of MPP4. Of note, similar effects were observed at 10 nM rapamycin (fig. S8C). Accordingly, rapamycin treatment restored in vitro the capacity of knockin MPP4 to differentiate into B cells when cultured on OP9/IL-7 stromal cells (Fig. 7G). We then determined the consequences of daily intraperitoneal injections for 2 weeks of 4 mg/kg rapamycin (61, 62) on the BM composition of WT and knockin mice with regards to HSPCs and mature lymphoid

and myeloid cells. Although chronic blockade of mTOR-dependent signaling induced no major changes in WT MPP4, it reversed the quantitative defect in knockin MPP4 and restored their mitochondrial activity (Fig. 7, H and I). This treatment also led to a slight expansion of LT-HSCs and the MPP1 subset but had no significant effect on LT-HSC, MPP2, or MPP3 numbers in 1013/1013 mice (fig. S8F). Rapamycin treatment did not correct the BM representation of CLPs and B cells nor the circulating lymphopenia in knockin mice, suggesting that the origin of the lymphopenia is likely multifactorial (Fig. 7J and fig. S8, F and G). Similarly, this treatment induced no major changes on the BM representation of CMPs, GMPs, MEPs, and mature myeloid cells (fig. S8, F and G). Collectively, these findings suggest a pivotal role for the Cxcr4-mTOR signaling axis in regulating the fate of MPP4 and their mitochondrial machinery.

DISCUSSION

This study was designed to determine whether and how proper CXCR4 desensitization controls the lymphoid versus myeloid specification of MPPs. We showed that Cxcr4 signaling coordinated the output of the lymphoid and myeloid lineages by regulating the composition and molecular identity of the MPP compartment. The MPP4 subset was pivotal in this Cxcr4-controlled process. Indeed, Cxcr4 desensitization was required for their efficient generation from MPP1 and then for their maintenance. Cxcr4 signaling seemed also necessary for MPP4 positioning near perivascular niches, and thereby likely for allowing access to external cues that shape their cell cycle status, their metabolism, and ultimately their fate. We also provided unanticipated evidence that Cxcr4 signaling regulates the fate decision of MPP4 through mTOR.

Our findings point towards disturbed HSPC generation and/or differentiation in BM as potential mechanisms contributing to WS-associated lymphopenia (37, 47, 63). This would explain, at least in part, why the lymphopenia can be normalized by chronic AMD3100

treatment in WS mice (this work) and patients (64). However, in vivo treatment with rapamycin did not correct the circulating lymphopenia in knockin mice despite normalizing the number of MPP4 in the BM and restoring their lymphoid potential in vitro, suggesting that mechanisms underlying the lymphoid rescue in AMD3100-treated mice might be multifactorial and could involve mobilization of lymphoid cells from peripheral tissues and/or modulation of cytokine production by BM stromal cells. Accordingly, Zehentmeier *et al.* reported that daily gavage with the CXCR4 antagonist X4P-X4-185-P1 restored IL-7 expression and rescued B-cell development in the BM of a WS mouse model bearing the *Cxcr4*^{R334X} mutation (65). We previously found that Cxcr4^{1013} knockin mice show dysregulation of the BM landscape, including reduced trabecular and cortical bone structures, and reported that intraperitoneal injections of AMD3100 increased the bone mass in Cxcr4^{1013} knockin mice by reversing the quantitative defect in skeletal cells and rescuing their osteogenic properties (60). Whether this partial normalization of the bone environment participates in the rescue of lymphoid compartment in AMD3100-treated mice deserves further investigations.

To date, 29 pathogenic *CXCR4* variants have been identified in WS patients, including nonsense, missense, and frameshift mutations (66, 67). All of them are positioned in the intracellular C-terminal domain of CXCR4. In all investigated variants, critical phospho-acceptor Ser and Thr sites needed for G protein–coupled receptor kinase (GRK)–mediated phosphorylation are removed, and this accounts for the failure of CXCR4 to be desensitized and internalized. These dysregulations contribute, together with abnormal β-arrestin–dependent signaling, to enhanced CXCL12-promoted chemotaxis in all investigated variants with the exception of the *CXCR4*^{Leu371fsX3} mutation (67, 68). A genotype-phenotype correlation study including 14 WS-associated *CXCR4* mutations reported a strong correlation between the degree of internalization defect with the severity of the leukopenia and the

recurrence of infections in WS patients (69). Moreover, the CXCR4 antagonist Mavorixafor prevented CXCL12-induced hyperactivation of ERK and AKT in vitro in all *CXCR4* variants. A phase 3 clinical trial conducted on 31 WS patients has shown that oral administration of Mavorixafor improves cytopenia and reduces the frequency and severity of infections (70, NCT03995108), leading to the approval of Mavorixafor as the first drug for WS by the FDA. Based on these observations, we can speculate that the phenotypes described in our study could be shared, at least in part, with other WS-associated *CXCR4* mutations. In accordance, a mouse model bearing the $Cxcr4^{R334X}$ mutation (the variant harbored by the two WS patients studied in this work) has been reported (65). Although this study did not address the impact of the mutation on early hematopoietic development, the authors showed, in agreement with our results, that this *Cxcr4* gain-of-function mutation was associated with altered B lymphopoiesis in BM including the CLP stage and reduced numbers of naive B cells in blood and secondary lymphoid organs.

Our transcriptomic analyses unveiled a role for Cxcr4 signaling in regulating the molecular identity of MPP4 and particularly their lymphoid-myeloid gene profile. Absence of Cxcr4 desensitization led to reduced accessibility of gene promoters associated with lymphocyte differentiation and decreased expression of key lymphoid differentiation genes in MPP4, whereas expression of pro-GM genes such as *Mpo* and *Irf8* were increased. Such imbalance in the lymphoid-myeloid gene landscape is likely at the origin of the myeloid skewing of knockin MPP4 we reported at the functional level in vitro and in vivo after transplantation. Moreover, we observed a reduction in Flt3, a phenotypic marker segregating MPP4 from MPP2/3, among knockin MPP4 at steady-state, and in vitro an increased recovery of $Flt3^{low}$ cells from knockin MPP4 cultures. These findings suggest that knockin MPP4 may undergo a molecular reprogramming that renders them phenotypically and functionally close to GM-biased MPP3. Finally, we showed that addition of Cxcl12 promotes in vitro myeloid

differentiation of WT MPP4, suggesting that the Cxcl12-Cxcr4 signaling axis also regulates the fate of MPP4 under physiological conditions. This further indicates that the abnormal myeloid fate phenotype observed in our Cxcr4 gain-of-function WS mouse model is in part due to the increase in Cxcr4 signaling interfering with the normal specification process of MPP4.

Investigating the BM localization of MPP subsets and their supporting niches remains a challenging issue, mainly due to their scarcity and the absence of specific surface markers. Lai *et al*. showed that lymphoid priming of MPPs requires homing of these cells to the inner region of the marrow, a process mediated by G protein–coupled receptor signaling (71). Cordeiro Gomes *et al*. reported that $Flt3^+$ MPPs resided in BM niches formed by IL-7^+ cells comprising perisinusoidal stromal cells and endothelial cells (34). Perivascular structures are reported to sustain HSPC maintenance and differentiation through secretion of Cxcl12, SCF, and IL-7 (26-28). Wu *et al*. reported in mouse sternum that all HSPCs, except MPP2 and myelo-erythroid progenitors, were enriched near megakaryocytes and that no HSPC subset preferentially localized to sinusoids or the endosteum when compared to random distributions. However, the distinction between MPP2 and myelo-erythroid progenitors and between MPP3, MPP4 and CMP was not established (30). Here, by combining in situ hybridization RNA-scope and immunofluorescence staining, we confirmed the quantitative defect in MPP4 in BM of knockin mice and further showed that proper Cxcr4 signaling is required for MPP4 positioning near peri-arteriolar structures that express Cxcl12. Reduction of phosphorylated STAT5α has been associated with defective positioning of CLPs and pro-B cells near IL-7^+ perivascular stromal cells (34, 52). Accordingly, our PhosphoFlow analyses revealed that impairment of Cxcr4 desensitization decreased STAT5α phosphorylation in MPP4 at baseline, thus supporting the hypothesis that the defective positioning of knockin MPP4 could affect access to critical niche factors controlling their fate, such as IL-7. Such mislocalization likely

exposed MPP4 to aberrant external cues, leading to defects in cell cycle status, mitochondrial activity, maintenance, and, ultimately, fate. Miao *et al.* showed that HSC homeostasis is balanced by the presence of Cxcr4 expressing progenitor cells in the niche, and particularly the MPP4 subset, due to competition for SCF produced by BM stromal cells (35). A major discovery from that study is the displacement of MPP4 and downstream hematopoietic progenitors from Cxcl12-producing niches in the BM through conditional *Cxcr4* deletion. That work points the MPP4 subset as pivotal in regulating HSPC homeostasis within the BM ecosystem by buffering access to extrinsic cues produced by the niches. In addition, Kang *et al*. identified a secretory subset of MPP3 that represents a novel bypass mechanism for rapid production of myeloid cells in inflammatory stress and disease conditions (29). This occurs through intrinsic lineage-priming and cytokine production in BM, thereby likely increasing myeloid cell production from other HSPC subsets including MPP4. Whether these changes are observed in the BM of our mouse model and how they would contribute to the lymphoid loss warrant further investigations. Together, these works and the present study illustrate how cell-extrinsic and -intrinsic mechanisms act together on MPP4 fate and how these processes depend on the integrity of the Cxcl12-Cxcr4 signaling.

Previous transcriptional and metabolomics studies suggested that MPP subsets are more dependent on OXPHOS for their metabolism than are HSCs (12, 24). Our findings revealed overactive OXPHOS-driven metabolism in Cxcr4^{1013} knockin MPP4. This was accompanied by increased ROS production, and, counterintuitively, by accumulation of damaged mitochondria with low mitochondrial membrane potential. This metabolically activated cell population was enriched in myeloid-primed cells and was more poised to give rise to myeloid progenies. Addition of Cxcl12 decreased the number of mitochondrial fragments and the membrane potential of WT MPP4 and this was reversed by AMD3100 treatment. In line with previous work reporting the capacity of Cxcl12 to regulate the

mitochondrial metabolism of mouse Lin^- BM cells (72), our study further extends its regulatory role to MPP4 under physiological conditions. In vitro examination of mTOR in Cxcl12-stimulated knockin MPP4 showed increased phosphorylation at Ser^{2448}, indicating an increase in mTOR activity. This was observed in $Cxcr4^{1013}$ knockin MPP4 with low TMRE content as well. Knockin MPP4 also displayed increased phosphorylation of downstream targets such as pS6 at $Ser^{235/236}$ and Akt at Ser^{473}, supporting the possibility that knockin MPP4 may adopt a state of increased metabolic activity including the mTOR pathway, compatible with high energy production and cycling. These responses were sensitive to AMD3100 and Rapamycin, thus suggesting that MPP4 may integrate local cues in BM including Cxcl12 signaling through Cxcr4 and then relayed them by the master regulator mTOR. Collectively, these findings lead us to propose that Cxcr4 acts intrinsically on MPP4, likely through the mTOR pathway, and extrinsically through niche-driven cues to regulate lymphoid cell fate in BM.

MATERIALS & METHODS

Healthy and WS donors and HSPC analyses

Investigations of human BM samples were performed in compliance with Good Clinical Practices and the Declaration of Helsinki. Cryopreserved BM aspirates from two WS patients (1 male, age 47 years; 1 female, age 30 years at sampling, both bearing the *CXCR4*^{R334X} mutation; collected under National Institutes of Health protocol 09-I-0200) were provided through a Material Transfer Agreement in accordance with National Institutes of Health human subject research policies. None of the patients were under specific treatments aiming at correcting their leukopenia such as G-CSF or CXCR4 antagonist treatments at the time of the BM collection. BM samples from four healthy donors that were matched for age and sex and used as control subjects were isolated from hip replacement surgery and stored in nitrogen. All individuals have provided written informed consent before sampling and data registering. The study was approved by the Comité de Protection des Personnes Ile-de-France VII (Protocol 17-030, n° ID-RCB: 2017-A01019-44). After sample thawing, BM phenotyping of HSPCs was performed as follows. In brief, 10^6 cells were labeled for 30 min at 4°C with a combination of the following conjugated antibodies: anti–human CD7 (clone M-T701, mouse IgG1, BD Biosciences 562635), CD10 (clone HI10A, mouse IgG1, BD Biosciences 562978), CD34 (clone 581, mouse IgG1, Biolegend 343510), CD38 (clone HIT2, mouse IgG1, BD Biosciences 555460), CD45RA (clone HI100, mouse IgG2b, BD Biosciences 560673), CD49f (clone GoH3, rat IgG2a, BD Biosciences 562475), CD135 (clone 4G8, mouse IgG1, BD Biosciences 563909) and CXCR4 (clone 12G5, mouse IgG2a, BD Biosciences 555975). Antibodies were conjugated to brilliant violet (BV) 421, BV605, BV650, PE, PE-cyanin (Cy) 5, peridinin chlorophyll protein PerCP/Cy5.5, alexa fluor (AF) 647 and AF700. Corresponding isotype- and species-matched antibodies were used as negative controls.

Mice and genotyping

Cxcr4$^{+/1013}$ (+/1013) mice were generated by a knock-in strategy and bred as described previously (36). *Cxcr4*$^{1013/1013}$ (1013/1013) mice were obtained by crossing heterozygous +/1013 mice. WT mice were used as a control. All mice were littermates and age matched (8–12 weeks-old). Adult Boy/J (CD45.1) (Charles River) mice were used as transplantation recipients and BM donors. *Cxcl12*$^{Ds\text{-}Red}$ knock-in mice (*DsRed-Express2* recombined into the *Cxcl12* locus) (27) were obtained from Dr L.G. Ng (Singapore Immunology Network, A*STAR, Singapore) and subsequently crossed with Cxcr4^{1013} knockin mice in our animal facility. All the mice were bred in our animal facility under a 12h light/dark cycle, specific pathogen-free conditions and fed ad libitum. All experiments were performed in accordance with the European Union guide for the care and use of laboratory animals and have been reviewed and approved by an appropriate institutional review committee (C2EA-26, Animal Care and Use Committee, Villejuif, France and Comité d'éthique Paris-Nord N°121, Paris, France).

Sample isolation

BM cells were extracted by centrifugation from intact femurs, tibia and hips to separate marrow and bone fractions. Cell collection was performed in Phosphate-Buffered Saline solution (PBS) 2% Fetal Bovine Serum (FBS) and filtered through a 70-µm nylon strainer to remove debris and fat. All cell numbers were standardized as total count per two legs. The peripheral blood was collected by submandibular puncture. Red blood cell lysis was performed using Ammonium-Chloride-Potassium (ACK) buffer. Analyses were carried out on an LSRII Fortessa flow cytometer (BD Biosciences) and data were analyzed with the FlowJo software (TreeStar).

Flow cytometry analyses

All staining analyses were performed on an LSR II Fortessa flow cytometer using the following antibodies: anti–mouse CD3 (clone 145-2C11, hamster IgG1, BD Biosciences 563565), CD4 (clone RM4-5, rat IgG2a, BD Biosciences 558107), CD11b (clone M1/70, rat IgG2b, BD Biosciences 557960), CD16/32 (clone 93, rat IgG2a, Sony Biotechnology 1106640), CD19 (clone 1D3, rat IgG2a, BD Biosciences 562291), CD34 (clone RAM34, rat IgG2a, eBioscience 48-0341-82), CD41 (clone MWReg30, rat IgG1, eBioscience 17-0411-82), CD45R/B220 (clone RA3-6B2, rat IgG2a, BD Biosciences 563894), CD45.1 (clone A20, mouse IgG2a, Sony Biotechnology 1153620), CD45.2 (clone 104, mouse IgG2a, eBioscience 12-0454-82), CD48 (clone HM48-1, Armenian hamster IgG, BioLegend 103412), CD117 (clone 2B8, rat IgG2b, BD Biosciences 553354), CD127 (clone A7R34, rat IgG2a, Sony Biotechnology 1275080), CD135 (clone A2F10, rat IgG2a, BD Biosciences 562537), CD150 (clone TC15-23F12,2, rat IgG2a, Sony Biotechnology 1179520), Ter119 (clone TER-119, rat IgG2b, Invitrogen A18447), Gr-1 (clone RB6-8C5, rat IgG2b, BioLegend 108412), Sca-1 (clone E13-161.7, rat IgG2a, Sony Biotechnology 1212570), Irf8 (clone V3GYWCH, mouse IgG1, eBioscience 12985282), Ackr3 (clone 8F11-M16, mouse IgG2b, BioLegend 331104) and Cxcr4 (clone 2B11, rat IgG2b, BD Biosciences 551966). Antibodies were conjugated to biotin, BV421, BV605, BV650, BV786, FITC, PE, APC, AF700, PE-Cy5, PE-Cy7, eFluor450, AF647, APC-eFluor780, peridinin chlorophyll protein PerCP-Cy5.5, or pacific blue. The lineage antibody cocktail included anti-CD3, anti-CD45R, anti-CD11b, anti-TER119, anti-CD41, and anti–Gr-1 mAbs (BD Biosciences 559971). Secondary labeling was performed with a Streptavidin–pacific orange or APC-Cy7 from Thermo Fisher Scientific. Data were analyzed with the FlowJo software (TreeStar, Ashland, OR).

Transplantation experiments and in vivo functional assays

For BM transplantation experiments, 1.5 x 10^6 total marrow cells from young CD45.2$^+$ WT, +/1013 or 1013/1013 mice were injected into lethally irradiated young CD45.1$^+$ WT recipient mice (two rounds of 5.5 Gy separated by 3 h). For competitive BM transplantation experiments, 1.5 x 10^6 total marrow cells from young CD45.2$^+$ WT, +/1013 or 1013/1013 mice were mixed with 1.5 x 10^6 total marrow cells from young CD45.1$^+$ WT mice (ratio 1:1). Mixture (3 x 10^6 cells) was injected into lethally irradiated young CD45.1/CD45.2$^+$ WT recipient mice (one round of 9 Gy). For reverse experiments, 1.5 x 10^6 total marrow cells from CD45.1$^+$ WT mice were injected into lethally irradiated CD45.2$^+$ WT or knockin recipient mice. Chimerism was analyzed 3 or 16 weeks after reconstitution. For in vivo differentiation assay, 10^4 MPP4 from CD45.2$^+$ WT, +/1013 or 1013/1013 mice were injected into sub-lethally irradiated CD45.1$^+$ WT recipient mice (one round of 4.5 Gy). BM and blood chimerism were analyzed 2 weeks after reconstitution by flow cytometry. For Cxcr4 blockade experiments, mice were daily injected intraperitoneally with 5 mg/kg AMD3100 (Sigma-Aldrich) or PBS during 3 weeks. Peripheral blood and BM were harvested 2 h after the last injection and analyzed by flow cytometry. For mTOR inhibition experiments, mice were daily injected intraperitoneally with 4 mg/kg Rapamycin (Sigma-Aldrich) or PBS for 2 weeks. Peripheral blood and BM were harvested 2 h after the last injection and analyzed by flow cytometry.

Cell cycle, survival, and metabolic assays

For cell cycle analyses, MPP1-4 from WT and knockin mice were permeabilized and fixed according to the manufacturer's instructions with the FOXP3 permeabilization kit (Foxp3/Transcription Factor Staining Buffer Set) and then labeled with Ki-67 antibody (clone B56, mouse IgG1; BD Biosciences 561277) and DAPI before flow cytometric analysis. For label-retaining assays (9, 37), mice were injected intraperitoneally with 180 µg BrdU (Sigma-

Aldrich) and maintained on water containing 800 µg/ml BrdU and 1% glucose during 12 days. The BrdU pulse was followed by a 3-weeks chase period to detect by flow cytometry label-retaining cells by combining surface staining to define MPPs with intracellular staining using the BrdU-FITC labeling kit following the manufacturer's instructions (BD Biosciences). Apoptosis was measured using the Annexin V detection kit (BD Biosciences) followed by DAPI staining as described previously (36, 73, 74). For mitochondria analysis, cells were incubated for 20 min at 37°C with tetramethylrhodamine-ethyl-esther (TMRE, 20 nM, Thermo Fisher) and MitoTrackerGreen (MTG, 100 nM, Thermo Fisher) before being analyzed by flow cytometry. Alternatively, MPP4 (0.5 x 10^3 cells/well in 96-well plates) were sorted into wells pre-seeded with 10^5 OP9 stromal cells and cultured for 24 h in DMEM supplemented with 10% FBS, 1% penicillin/streptomycin, and in presence or absence of Cxcl12 (1-10 nM) and AMD3100 (10 µM). OP9 stromal cells were obtained from Dr. I. André-Schmutz (Institut Imagine, Paris, France) (75). Cells were then harvested, incubated for 20 min at 37°C with TMRE and MTG before being analyzed by flow cytometry. Analysis of TFAM was performed as previously described (57) with minor modifications. In brief, 7 x 10^3 cells were incubated at 4°C for 30 min with surface antibodies required to define MPPs before being permeabilized with ice-cold methanol at -20°C for 20 min. After one wash with PBS-2%FBS, cells were incubated with monoclonal rabbit anti-mouse TFAM antibody (Abcam ab252432) at room temperature (RT) for 30 min. Cells were then washed, incubated with goat anti-Rabbit IgG antibody at RT for 30 min before being analyzed by flow cytometry.

Multiplex qPCR

Multiplex qPCR analysis was performed using the microfluidic Biomark system. Bulks of 0.1 x 10^3 MPP4 or single $TMRE^{low}$ MPP4 were sorted directly into PCR tubes containing 5 µl of

reverse transcription/pre-amplification mix as described (76). Briefly, the mix contained 2X reaction buffer and SuperScriptIII provided by CellsDirect One-Step qRT–PCR kit (Invitrogen) and 0.2X Taqman assay (Life technologies). Targeted cDNA pre-amplification was performed during 21 (single-cell analyses) or 22 cycles (bulk analyses) and pre-amplified product was diluted 1:5 in TE buffer before processing with Dynamic Array protocol according to the manufacturer's instructions (Fluidigm). Cells expressing *Actb* and controls genes (*Flt3*, *Cd48*, *Slamf1* and *Irf8*) and not *Pax5* and/or *Cd3* (negatives controls) were considered for further analyses (table S2). Expression of *Actb* was used for normalization. Heatmaps were generated with http://www.heatmapper.ca (77) using Z scores and principal component analysis (PCA) with R software using edgeR package.

RNA-seq

For RNA-seq data, pools of 3 x 10^3 MPP1-4 were sorted directly into RLT buffer (Qiagen) enriched with 1% of β-mercaptoethanol. Total RNA isolation and DNAse treatment were performed using RNeasy Micro Kit (Qiagen). Full length cDNAs were generated from 350 to 1,000 pg of total RNA using Clontech SMART-Seq v4 Ultra Low Input RNA kit for Sequencing (Takara Bio Europe, Saint Germain-en-Laye, France) according to manufacturer's instructions with 12 cycles of PCR for cDNA amplification by Seq-Amp polymerase. Six hundred pg of pre-amplified cDNAs were then used as input for Tn5 transposon tagmentation by the Nextera XT DNA Library Preparation Kit (96 samples) (Illumina, San Diego, CA) followed by 12 cycles of library amplification. Following purification with Agencourt AMPure XP and SPRIselect beads (Beckman-Coulter, Villepinte, France), the size and concentration of libraries were assessed by capillary electrophoresis. Sequencing reads (50 bp) were generated on the GenomEast platform (Illumina). RNA-seq libraries have been sequenced in Paired-End mode. Briefly, reads were preprocessed in order to remove adapter

and low-quality sequences (Phred quality score below 20) and reads shorter than 40 bases were discarded for further analysis. Reads were mapped onto the mm10 assembly of Mus musculus genome using STAR (78). Gene expression quantification was performed from uniquely aligned reads using htseq-count (79) with annotations from Ensembl and "union" mode. Only non-ambiguously assigned reads have been retained for further analyses. Read counts have been normalized across samples with the median-of-ratios method proposed by Anders and Huber (80), to make these counts comparable between samples. Genes expressed in at least 2 biological replicates were considered for further analyses, whereas 10% of genes with the lowest expression in WT and knockin MPPs summed up were excluded. Differentially expressed genes were identified with edgeR package. Volcano plots were generated with logFC and adjusted p-value (Benjamini-Hotchberg) returned by edgeR. Plots were generated with ggplot2 under R version 4.2.1. For GSEA analysis, we used the standard GSEA desktop version 4.3.2. All genes were submitted to GSEA, along with their expression, and ranked by SignalToNoise Metric. Standard parameters were used: 1000 gene set permutations, sets larger than 500 and smaller that 15 were excluded. Standard GSEA multiple testing correction was computed and retained for analysis (column q-value returned by the software). GO analyses have been performed using https://biit.cs.ut.ee/gprofiler (81) using a significance threshold of 0.05 as determined by Benjamini-Hochberg method. Data are available in GEO: GSE182992.

ATAC-seq

ATAC-seq was performed as previously described (82) with some modifications. Briefly, 10^4 to 3 x 10^4 cells were spun at 500g for 5 min, washed with cold PBS, lysed in cold lysis buffer (10 mM Tris-HCl, pH 7.5, 10 mM NaCl, 3 mM MgCl2 and 0.1% NP-40, 0.1% Tween-20 and 0.01% Digitonin), incubated 3 min on ice, resuspended in wash buffer (10 mM Tris-HCl, pH

7.5, 10 mM NaCl, 3 mM MgCl2, 0.1% Tween-20) and spun at 500g for 10 min at 4°C. The pelleted nuclei were resuspended in 50 µl transposase reaction mix (1X Diagenode Tagmentation buffer (Diagenode C01019043), 0,1% Tween-20, 0.01% Digitonin, 1.7ug Tn5 (Diagenode C01070010) previously loaded with nextera adapters loaded) for 30 min at 37°C on thermomixer shaking at 1000 rpm. Transposed DNA was purified using a DNA Clean & Concentrator-5 kit (Zymo Research) in 10 µl nuclease-free H2O and amplified with NEBNext® High-Fidelity 2X PCR Master Mix and 1 ul of primer pair from Diagenode (24 SI for tagmented libraries, C01011032), using the following PCR conditions: 72°C for 5 min; 98°C for 30 s then 12 cycles of 98°C for 10 s, 63°C for 30 s and 72°C for 1 min. Libraries were purified and size selected (1.4X-0.5X-1X successively) with AMPure XP beads (Beckman Coulter) then subjected to high-throughput paired-end sequencing (75bp) using the Illumina NextSeq500 sequencer (Illumina, San Diego, CA). Alignment, quality control, peak calling and reproducibility were assessed using ENCODE ATAC-seq analysis pipeline (https://github.com/ENCODE-DCC/atac-seq-pipeline). Briefly, sequencing reads were aligned to the mouse mm10 version of the genome using Bowtie2 (83), duplicate reads marked with Picard Tools and removed, and accessibility peaks were called using MACS2 (84) using default options. BigWig files normalized for the depth of sequencing of aligned filtered reads were generated using deeptools (85). Differential enrichment analysis was performed using diffReps (86) on replicated data using negative binomial statistical test using following parameters: --meth nb --mode p --nsd s --frag 250. Mode p corresponds to the scanning mode: (p)eak (=1000) Histone mark peak, nsd s corresponds to Z-score cutoff for low read count: (s)harp (=20) and frag 250 corresponds to the ChIP-seq library fragment size and was used to shift read positions. Regions with an abs(log2FoldChange) ≥ 0.8 and an adjusted p-value ≤ 0.001 (determined using the Benjamini-Hochberg method) were kept for downstream analysis. Differential regions annotation and Gene Ontology analysis was

performed using GREAT software (http://great.stanford.edu/public/html/) (87). Gene Ontology genesets are from Gene Ontology Biological Process geneset collection. Motif enrichment analysis was performed using Homer v4.11 (88) (findMotifsGenome.pl) on ATAC-seq peaks significantly decreased or increased (log2FC >= 0.8, pvalue <= 10-5) in 1013/1013 MPP1 or MPP4 compared to WT using the following parameters: mm10 -size 600. Data are available in GEO: GSE271225.

In vitro functional assays

Cxcr4 internalization assay was performed as previously described (36, 37) with some minor modifications. In brief, 1 x 10^6 BM cells were incubated at 37°C or 4°C for 45 min with or without Cxcl12 (10 nM, R&D Systems). The reaction was stopped by adding ice-cold RPMI and brief centrifugation at 4°C. After one wash in acidic glycine buffer, pH 4.3, Cxcr4 membrane expression was determined by flow cytometry using the additional markers CD3, CD45R, Gr1, CD11b, Ter119, CD41, CD117, Sca-1, Flt3, CD48 and CD150 antigens. Background fluorescence was evaluated using the corresponding PE-conjugated immunoglobulin-isotype control antibody. Cxcr4 expression in stimulated cells was calculated as follows: (Cxcr4 geometric MFI of treated cells/Cxcr4 geometric MFI of unstimulated cells) × 100; 100% correspond to receptor expression at the surface of cells incubated in medium alone. For chemotaxis assays, preliminary enrichment in Lin^- cells was performed using a HSPC enrichment set (BD Biosciences). 1 x 10^6 of cells were then diluted in 150 µl of DMEM supplemented with 0.5% BSA and 10 mM HEPES and incubated for 45 min at 37°C before being allowed to migrate through a 6.5 mm diameter, 5 µm pore polycarbonate Transwell culture insert (Corning). The same media (450 µl) with or without 10 nM of Cxcl12 was placed in the lower chamber. When specified, the Cxcr4 antagonist AMD3100 (10 µM, Sigma-Aldrich) was added in both upper and lower chambers. Input cells

that migrated to the lower chamber after 3 h of incubation at 37°C in humidified air with 5% CO_2 were collected, stained with CD3, B220, Gr1, Ter119, CD117, Sca-1, CD48, CD150 and Flt3 antibodies and counted by flow cytometry. The fraction of cells migrating across the polycarbonate membrane was calculated as follows: [(number of cells migrating to the lower chamber in response to chemokine or medium) / (number of cells added to the upper chamber at the start of the assay)] x 100. For Phosphoflow analyses of mTOR, Akt and S6, 7 x 10^6 of total BM cells were pre-incubated in DMEM only with or without 10 µM of AMD3100 during 1 h before being stimulated with 20 nM Cxcl12 during 5 min at 37°C. Cells were then stained with CD3, B220, Gr1, Ter119, CD117, Sca-1, CD48, CD150 and Flt3 antibodies. Phosphoflow stainings have been performed using the Perfix EXPOSE Kit (Beckman-Coulter) according to the manufacturer's instructions and Phospho-mTOR (Ser^{2448}) (clone MRRBY, mouse IgG2a, eBioscience 12971842), Phospho-Akt (Ser^{473}) (clone M89-61, mouse IgG1, BD Biosciences 562465) and Phospho-S6 ($Ser^{235/236}$) (clone D57.2.2E, rabbit IgG, Cell Signaling Technology 4851) antibodies. For Phosphoflow analyses of p38 and STAT5α, sorted 10^3 MPP4 were pre-incubated in DMEM only with or without 10 µM of AMD3100 during 1 h before being stimulated with 20 nM Cxcl12 during 2 min at 37°C. Phosphoflow staining have been performed using the Perfix EXPOSE Kit and Phospho-p38 (Thr^{180}/Tyr^{182}) (clone 36/p38 (pT180/pY182), mouse IgG1, BD Biosciences 563569) and Phospho-STAT5α (Tyr694) (clone 47/Stat5(pY694), mouse IgG1, BD Biosciences 562076) antibodies. Negative controls omitting Phospho-Abs were performed to ensure the robustness of the staining. For in vitro hematopoietic differentiation experiments, sorted ST-HSCs/MPP1 or MPP4 were seeded at 0.5 x 10^3 cells into a 96-well tissue culture plate in DMEM medium supplemented with 10% FBS, 1% penicillin/streptomycin, and the following murine cytokines (5, 10, or 50 ng/mL): SCF, IL-3, IL-6, IL-7, and Flt3-L (PeproTech) in the presence or absence of Cxcl12 (100 nM), AMD3100 (10 nM or 10 µM), Rapamycin (10 or 250 nM), 10 nM Mito-q, 5 µM

CCCP or 200 µM NAC. Cells were cultured at 37°C in a humidified atmosphere containing 5% CO_2 and were harvested at the indicated intervals to be analyzed by flow cytometry after staining with CD3, B220, Gr1, CD11b, Ter119, CD117, Sca-1, CD48, CD150, Flt3, CD16/32 and CD34 antibodies. For lymphoid differentiation assays, MPP1, MPP3 or MPP4 (0.5 x 10^3 cells/well in 96-well plates) were isolated from BM or sorted from MPP1 cultures into wells pre-seeded with 10^5 OP9 stromal cells. As described (10), cells were cultured in OptiMEM (Invitrogen) supplemented with 5% FBS, 1% penicillin/streptomycin, and the following murine cytokines: SCF (10 ng/mL), Flt3-L (10 ng/mL) and IL-7 (5 ng/mL) in the presence or absence of 10 µM AMD3100 or 250 nM Rapamycin. After sequential withdrawal of Flt3-L (day 3) and SCF (day 5), cells were maintained with IL-7 until 7 days of culture. Cells were then harvested and analyzed by flow cytometry after staining with CD11b and B220 antibodies. For Seahorse metabolic flux experiments, OCR and ECAR were measured using an 8-well Seahorse XFp Analyzer according to manufacturer's instructions (Agilent Technologies). In brief, MPP4 (7 x 10^4 cells per well) were sorted directly into 8-well plates pre-coated with poly-lysine (Sigma-Aldrich) and containing XF DMEM medium. Plates were then centrifuged and immediately analyzed following manufacturer's instructions. For measurement of glucose uptake and ROS abundance, 2 x 10^3 purified MPP4 were seeded into a 96-well tissue culture plate in DMEM medium supplemented with 10% FBS, 1% penicillin/streptomycin. After 4 h of culture, cells were washed with DMEM and incubated for 20 min at 37°C with MitoSox (5 µM, Thermo Fisher Scientific), CellRox DeepRed (1.25 µM, Thermo Fisher Scientific) and dichlorofluorescin diacetate (DCFDA, 10 µM, Thermo Fisher Scientific) to measure ROS content by flow cytometry. For glucose uptake experiments, the medium was supplemented with 100 µM of 2-NBD-Glucose (Abcam) at the start of the assay and the incorporation of this fluorescent analog has been measured by flow cytometry after 4 and 20 h of culture.

In situ RNA hybridization and immunofluorescence microscopy

For analyses of BM localization of MPP4 by in situ RNA hybridization and immunofluorescence microscopy, freshly dissected mouse femurs were fixed overnight in 4% ParaFormAldehyde (PFA) followed by 48 h decalcification in EDTA (0.5 M, pH=7.4) under agitation at 4°C. Bones were incubated overnight in PBS 1X containing 20% sucrose (Sigma) and 2% polyvinylpyrrolidone (PVP) (Sigma) at 4°C. The embedding was performed using Sub Xero freezing media (Mercedes Medical) before storing the samples at -80°C. Bones were sectioned (14 µm-thick) using a cryostat (Thermofisher). RNA-Scope was performed using the RNAscope® Multiplex Fluorescent Detection Kit v2 kit (323110, ACD) and RNAscope® H_2O_2 and protease Reagents kit (322381, ACD) according to the manufacturer's instructions. Briefly, tissue sections were rehydrated in PBS 1X for 5 min at RT, incubated 30 min at 60°C in a HybEZ II oven and fixed for 15 min at 4°C in 4% PFA. Tissue sections were treated with H_2O_2 for 10 min at RT followed by incubation in target retrieval reagents solution for 11 min at 90°C and protease III solution for 30 min at 40°C. Then, sections were incubated with targeted probes: Flt3 (487861 RNAscope® Probe - Mm-Flt3 - musculus FMS-like tyrosine kinase 3 (Flt3) mRNA), c-Kit (314151-C2 RNAscope® Probe Mm-Kit-C2), positive probe (LOT: 2018452 RNAscope® 3-plex positive control probe-Mm) and negative probe (LOT: 21285A RNAscope® 3-plex negative control Probe). The hybridization procedure was performed for 2 h at 40°C. Sequential amplification steps were performed according to manufacturer's instructions using Amp1, Amp2 and Amp3 solutions at 40°C. Finally, tissue sections were incubated with Opal570 (OP-001003 Bio-thechne R&D) and Opal650 (OP-001005 Bio-thechne R&D) for 30 min at 40°C. RNA in situ hybridization was followed by an immunofluorescence overnight staining using the primary anti-mSca-1/Ly6 antibody (AF1226 Bio-thechne R&D). Laminin positive structures were identified by an

immunofluorescence overnight staining using the primary anti-Laminin antibody (L9393 Sigma). Then, sections were incubated with the appropriate secondary antibodies Donkey anti-goat AF488 (A-11055 Thermofisher) and Donkey anti-Rabbit IgG (H+L) Highly Cross-Adsorbed Secondary Antibody, AF680 (A-10043 Thermofisher) for 75 min at RT with DAPI for nuclear staining. Autofluorescence was removed with the True Black Kit (92401 TrueBlack® Lipofuscin Autofluorescence Quencher) according to the manufacturer's instructions. Mounting was performed using the mounting media ProLong Gold antifade reagent (P36934 Invitrogen). Images were acquired using a LSM780 confocal microscope and processed using the open-source digital image analysis software QuPath v0.2.3 (89). Integration of ImageJ (90) package allowed the total cell detection. Sca-1$^+$ cell detection and classification were assessed by using the Qupath detection and classification tools. Subcellular detection was performed within the Sca-1$^+$ cells to classify MPP4 as Sca-1$^+$, Flt3$^+$, c-Kit$^+$ cells. Laminin detection was performed by pixel classification tool. Distance was calculated from each cell classified as a MPP4 cell to the nearest Laminin$^+$, Sca-1$^+$ cells by spatial analysis in Qupath using the detectionToAnnotationDistances tool. Nearest Neighbor Index was used to detect clustering patterns in point patterns obtained from coordinates of cells detected with the Qupath software. The Nearest Neighbor Index (NNI) quantifies the extent of regularity or randomness in the distribution of a set of points (91). Mathematically, the NNI is represented as: NNI = $\frac{\bar{r}}{\bar{e}}$. Here, $\bar{r}$ is the average observed distance from one point to its nearest neighboring point in the dataset. On the other hand, $\bar{e}$ is the expected average nearest neighbor distance if the points were distributed randomly within the study area. This expected distance is derived from the formula: $\bar{e} = \frac{0.5}{\sqrt{n/A}}$. Where n stands for the number of points, and A represents the total area encompassed by the study. Interpreting the NNI, a value close to 1 suggests the points are randomly distributed. A value significantly less than 1 indicates a clustered arrangement, and conversely, a value greater than 1 is indicative of a more regular

or uniform distribution. Spatial coordinates of points were obtained from the centroids of the cells of interest detected with the Qupath software. Using the spatstat package in R, we processed these coordinates to compute the nearest neighbor distances (92). This data, along with the total study area, enabled the calculation of the NNI.

For mitochondria network analysis by immunofluorescence, 5 x 10^3 MPP4 were sorted directly into 24-well plates containing coverslips pre-coated with poly-l-lysine. Alternatively, MPP4 were seeded at 5 x 10^3 cells into a 96-well tissue culture plate in DMEM medium supplemented with 10% FBS, 1% penicillin/streptomycin, in the presence or absence of Cxcl12 (1-100 nM) for 24 h. Cells were then transferred to 24-well plates containing coverslips pre-coated with poly-l-lysine. After 2 h incubation at 37°C in order to allow cell adhesion to the coverslips, the cells were fixed using PBS 4% PFA. Fixed cells were permeabilized with PBS 0.3% Triton X for 10 min, extensively washed and blocked with PBS 1% BSA for 1 h at RT. The MPP4 were then incubated with unlabeled primary TOMM20 (1 µg/mL, Rabbit IgG, Thermo Fisher Scientific) antibody overnight at 4°C, followed by wash and incubation with secondary antibody (1 µg/mL, Goat anti-Rabbit IgG, Thermo Fisher Scientific) and the nuclear dye Hoechst 33342 during 1h at RT (table S3). After mounting the slides using ProLong™ Gold Antifade mounting medium (Thermo Fisher Scientific), the images were obtained with a Plan-Apochromatic objective (63x oil-immersion objective with a numerical aperture of 1.4) using the LSM800 confocal microscope (Carl Zeiss). Sections were acquired as serial z stacks (0.56 µm apart) and were subjected to maximum intensity projection in the Zen 2.3 System software. Brightness and contrast settings were set during capture and not altered for analysis. Mitochondrial labeling were individualized for each confocal optical slice and the number of fragments were calculated using the 'Analyze Particles' plug-in on thresholded images in Fiji software using a threshold of 4483 and a filter of 0.6µm^2 for the minimum size of the fragments. A macro enabling the automatic

quantification of a batch of images is available upon request. At least 50 cells/condition were analyzed. Box plots show the median, and cover the interquartile range (IQR) between the first and the third quartiles (Q1 and Q3). Whiskers are drawn at the extreme value that is no more than Q3+1.5xIQR, and no less than Q1-1.5xIQR with outliers shown as black dot.

Statistical analyses

Data are expressed as mean ± SEM. Statistical analyses were conducted using Prism software (GraphPad Software) or R software Kruskal Wallis tests were used to determine if there were differences among WT, +/1013 and 1013/1013 within MPP1-4, followed by pair-wise Dunn's test if appropriate. For each panel, all pairwise comparisons were performed but only the significant ones ($P < 0.05$) are indicated in the figures at the exception of certain panels where we indicated the exact P value.

SUPPLEMENTARY MATERIALS

Figs S1–S7.

Tables S1–S3

Data Files S1–S12.

REFERENCES AND NOTES

1. Orkin SH, Zon LI. Hematopoiesis: an evolving paradigm for stem cell biology. *Cell.* 2008;132(4):631-44.
2. Doulatov S, Notta F, Laurenti E, Dick JE. Hematopoiesis: a human perspective. *Cell Stem Cell.* 2012;10(2):120-36.
3. Ema H, Morita Y, Suda T. Heterogeneity and hierarchy of hematopoietic stem cells. *Exp Hematol.* 2014;42(2):74-82.e2.

4. Simsek T, Kocabas F, Zheng J, et al. The distinct metabolic profile of hematopoietic stem cells reflects their location in a hypoxic niche. *Cell Stem Cell.* 2010;7(3):380-90.
5. Takubo K, Nagamatsu G, Kobayashi CI, et al. Regulation of glycolysis by Pdk functions as a metabolic checkpoint for cell cycle quiescence in hematopoietic stem cells. *Cell Stem Cell.* 2013;12(1):49-61.
6. Zhong RK, Astle CM, Harrison DE. Distinct developmental patterns of short-term and long-term functioning lymphoid and myeloid precursors defined by competitive limiting dilution analysis in vivo. *J Immunol.* 1996;157(1):138-45.
7. Sun J, Ramos A, Chapman B, et al. Clonal dynamics of native haematopoiesis. *Nature.* 2014;514(7522):322-7.
8. Busch K, Klapproth K, Barile M, et al. Fundamental properties of unperturbed haematopoiesis from stem cells *in vivo*. *Nature.* 2015;518(7540):542-6.
9. Wilson A, Laurenti E, Oser G, et al. Hematopoietic stem cells reversibly switch from dormancy to self-renewal during homeostasis and repair. *Cell.* 2008;135(6):1118-29.
10. Pietras EM, Reynaud D, Kang Y-A, et al. Functionally Distinct Subsets of Lineage-Biased Multipotent Progenitors Control Blood Production in Normal and Regenerative Conditions. *Cell Stem Cell.* 2015;17(1):35-46.
11. Sommerkamp P, Romero-Mulero MC, Narr A, et al. Mouse multipotent progenitor 5 cells are located at the interphase between hematopoietic stem and progenitor cells. *Blood*. 2021;137(23):3218-3224.
12. Cabezas-Wallscheid N, Klimmeck D, Hansson J, et al. Identification of regulatory networks in HSCs and their immediate progeny via integrated proteome, transcriptome, and DNA methylome analysis. *Cell Stem Cell.* 2014;15(4):507-522.
13. Urbanus J, Cosgrove J, Beltman JB, et al. DRAG in situ barcoding reveals an increased number of HSPCs contributing to myelopoiesis with age. *Nat Commun*. 2023;14(1):2184.

14. Lai A, Kondo M. Asymmetrical lymphoid and myeloid lineage commitment in multipotent hematopoietic progenitors. *J Exp Med*. 2006;203(8):1867-73.
15. Itoh-Nakadai A, Matsumoto M, Kato H, et al. A Bach2-Cebp Gene Regulatory Network for the Commitment of Multipotent Hematopoietic Progenitors. *Cell Rep*. 2017; 18(10):2401-2414.
16. Lenaerts A, Kucinski I, Deboutte W, et al. EBF1 primes B-lymphoid enhancers and limits the myeloid bias in murine multipotent progenitors. *J Exp Med*. 2022;219(11):e20212437.
17. Maryanovich M, Zaltsman Y, Ruggiero A, et al. An MTCH2 pathway repressing mitochondria metabolism regulates haematopoietic stem cell fate. *Nat Commun.* 2015;6: 7901.
18. Luchsinger LL, Justino de Almeida M, Corrigan DJ, et al. Mitofusin 2 maintains haematopoietic stem cells with extensive lymphoid potential. *Nature.* 2016;529(7587):528-31.
19. Ho TT, Warr MR, Adelman ER, et al. Autophagy maintains the metabolism and function of young and old (hematopoietic) stem cells. *Nature.* 2017;543(7644):205-210.
20. Agathocleous M, Meacham CE, Burgess RJ, et al. Ascorbate regulates haematopoietic stem cell function and leukaemogenesis. *Nature*. 2017;549(7673):476-481.
21. DeVilbiss AW, Zhao Z, Martin-Sandoval MS, et al. Metabolomic profiling of rare cell populations isolated by flow cytometry from tissues. *Elife*. 2021;10:e61980.
22. Bonora M, Ito K, Morganti C, et al. Membrane-potential compensation reveals mitochondrial volume expansion during HSC commitment. *Exp Hematol*. 2018;68:30-37.e1.
23. Jun S, Mahesula S, Mathews TP, et al. The requirement for pyruvate dehydrogenase in leukemogenesis depends on cell lineage. *Cell Metab*. 2021;33(9):1777-1792.e8.

24. Schönberger K, Obier N, Romero-Mulero MC, et al. Multilayer omics analysis reveals a non-classical retinoic acid signaling axis that regulates hematopoietic stem cell identity. *Cell Stem Cell*. 2022;29(1):131-148.e10.
25. Zhao M, Li L. Dissecting the bone marrow HSC niches. *Cell Res*. 2016;26(9):975-6.
26. Ding L, Saunders TL, Enikolopov G, et al. Endothelial and perivascular cells maintain haematopoietic stem cells. *Nature*. 2012;481(7382):457-62.
27. Ding L, Morrison SJ. Haematopoietic stem cells and early lymphoid progenitors occupy distinct bone marrow niches. *Nature*. 2013;495(7440):231-5.
28. Miao R, Lim VY, Kothapalli N, et al. Hematopoietic Stem Cell niches and signals controlling immune cell development and maintenance of immunological memory. *Front Immunol*. 2020;11:600127.
29. Kang Y-A, Paik H, Zhang SY, et al. Secretory MPP3 reinforce myeloid differentiation trajectory and amplify myeloid cell production. *J Exp Med*. 2023;220(8):e20230088.
30. Wu Q, Zhang J, Kumar S, et al. Resilient anatomy and local plasticity of naive and stress haematopoiesis. *Nature*. 2024;627(8005):839-846.
31. Reynaud D, Pietras E, Barry-Holson K, et al. IL-6 controls leukemic multipotent progenitor cell fate and contributes to chronic myelogenous leukemia development. *Cancer Cell.* 2011;20(5):661-73.
32. Pietras EM, Mirantes-Barbeito C, Fong S, et al. Chronic interleukin-1 exposure drives haematopoietic stem cells towards precocious myeloid differentiation at the expense of self-renewal. *Nat Cell Biol*. 2016;18(6):607-18.
33. Yamashita M, Passegué E. TNF-α Coordinates Hematopoietic Stem Cell Survival and Myeloid Regeneration. *Cell Stem Cell.* 2019;25(3):357-372.e7.

34. Gomes AC, Hara T, Lim VY, et al. Hematopoietic Stem Cell Niches Produce Lineage-Instructive Signals to Control Multipotent Progenitor Differentiation. *Immunity.* 2016;45(6):1219-1231.
35. Miao R, Chun H, Feng X, et al. Competition between hematopoietic stem and progenitor cells controls hematopoietic stem cell compartment size. *Nat Commun*. 2022;13(1):4611.
36. Balabanian K, Brotin E, Biajoux V, et al. Proper desensitization of CXCR4 is required for lymphocyte development and peripheral compartmentalization in mice. *Blood.* 2012;119(24):5722–30.
37. Freitas C, Wittner M, Nguyen J, et al. Lymphoid differentiation of hematopoietic stem cells requires efficient Cxcr4 desensitization. *J. Exp. Med.* 2017;214(7):2023–2040.
38. Laurenti E, Doulatov S, Zandi S, et al. The transcriptional architecture of early human hematopoiesis identifies multilevel control of lymphoid commitment. *Nat Immunol.* 2013;14(7):756-63.
39. Notta F, Zandi S, Takayama N, et al. Distinct routes of lineage development reshape the human blood hierarchy across ontogeny. *Science.* 2016;351(6269):aab2116.
40. Buenrostro JD, Corces MR, Lareau CA, et al. Integrated Single-Cell Analysis Maps the Continuous Regulatory Landscape of Human Hematopoietic Differentiation. *Cell*. 2018;173(6):1535-1548.e16.
41. Ben-David Y, Gajendran B, Sample KM, Zacksenhaus E. Current insights into the role of Fli-1 in hematopoiesis and malignant transformation. *Cell Mol Life Sci*. 2022;79(3):163.
42. Ng AP, Coughlan HD, Hediyeh-zadeh S, et al. An Erg-driven transcriptional program controls B cell lymphopoiesis. *Nat Commun*. 2020;11(1):3013.
43. Xue HH, Bollenbacher-Reilly J, Wu Z, et al. The transcription factor GABP is a critical regulator of B lymphocyte development. *Immunity*. 2007;26(4):421-31.

44. Chavez JS, Rabe JL, Niño KE, et al. PU.1 is required to restrain myelopoiesis during chronic inflammatory stress. *Front Cell Dev Biol*. 2023:11:1204160.
45. Wang C, Tu Z, Cai X, et al. A critical role of RUNX1 in governing megakaryocyte-primed hematopoietic stem cell differentiation. *Blood Adv*. 2023;7(11):2590-2605.
46. Young K, Borikar S, Bell R, et al. Progressive alterations in multipotent hematopoietic progenitors underlie lymphoid cell loss in aging. *J. Exp. Med.* 2016;213(11):2259-2267.
47. McDermott DH, Gao J-L, Liu Q, et al. Chromothriptic cure of WHIM syndrome. *Cell.* 2015;160(4):686-699.
48. Gao J-L, Yim E, Siwicki M, et al. Cxcr4-haploinsufficient bone marrow transplantation corrects leukopenia in an unconditioned WHIM syndrome model. *J Clin Invest*. 2018;128(8):3312-3318.
49. Bonaud A, Lemos JP, Espéli M, Balabanian K. Hematopoietic Multipotent Progenitors and Plasma Cells: Neighbors or Roommates in the Mouse Bone Marrow Ecosystem? *Front Immunol*. 2021;12:658535.
50. Kunisaki Y, Bruns I, Scheiermann C, et al. Arteriolar niches maintain haematopoietic stem cell quiescence. *Nature*. 2013;502(7473):637-43
51. Nombela-Arrieta C, Pivarnik G, Winkel B, et al. Quantitative imaging of haematopoietic stem and progenitor cell localization and hypoxic status in the bone marrow microenvironment. *Nat Cell Biol*. 2013;15(5):533-43.
52. Balzano M, De Grandis M, Vu Manh T-P, et al. Nidogen-1 Contributes to the Interaction Network Involved in Pro-B Cell Retention in the Peri-sinusoidal Hematopoietic Stem Cell Niche. *Cell Rep*. 2019;26(12):3257-3271.e8.
53. Paul F, Arkin Y, Giladi A, et al. Transcriptional Heterogeneity and Lineage Commitment in Myeloid Progenitors. *Cell.* 2015;163(7):1663-77.

54. Sasaki H, Kurotaki D, Osato N, et al. Transcription factor IRF8 plays a critical role in the development of murine basophils and mast cells. *Blood.* 2015;125(2):358-69.
55. Möröy T, Vassen L, Wilkes B, Khandanpour C. From cytopenia to leukemia: the role of Gfi1 and Gfi1b in blood formation. *Blood*. 2015;126(24):2561-2569.
56. Yu W-M, Liu X, Shen J, et al. Metabolic regulation by the mitochondrial phosphatase PTPMT1 is required for hematopoietic stem cell differentiation. *Cell Stem Cell.* 2013;12(1): 62-74.
57. Justino de Almeida M, Luchsinger LL, Corrigan DJ et al. Dye-Independent Methods Reveal Elevated Mitochondrial Mass in Hematopoietic Stem Cells. *Cell Stem Cell*. 2017; 21(6):725-729.
58. Goldberg MS, Fleming SM, Palacino JJ, et al. Parkin-deficient mice exhibit nigrostriatal deficits but not loss of dopaminergic neurons. *J Biol Chem.* 2003;278(44):43628-35.
59. Recasens-Zorzo C, Cardesa-Salzmann T, Petazzi P, et al. Pharmacological modulation of CXCR4 cooperates with BET bromodomain inhibition in diffuse large B-cell lymphoma. *Haematologica*. 2019;104(4):778-788.
60. Anginot A, Nguyen J, Abou Nader Z, et al. WHIM Syndrome-linked CXCR4 mutations drive osteoporosis. *Nat Commun*. 2023;14(1):2058.
61. Chen C, Liu Yu, Liu Ya, Zheng P. mTOR Regulation and Therapeutic Rejuvenation of Aging Hematopoietic Stem Cells. *Sci Signal*. 2009;2(98):ra75.
62. Fujino T, Goyama S, Sugiura Y, et al. Mutant ASXL1 induces age-related expansion of phenotypic hematopoietic stem cells through activation of Akt/mTOR pathway. *Nat Commun*. 2021;12(1):1826.
63. Kriván G, Erdos M, Kállay K, et al. Successful umbilical cord blood stem cell transplantation in a child with WHIM syndrome. *Eur J Haematol.* 2010;84(3):274-5.

64. McDermott DH, Liu Q, Velez D, et al. A phase 1 clinical trial of long-term, low-dose treatment of WHIM syndrome with the CXCR4 antagonist plerixafor. *Blood.* 2014;123(15):2308-16.

65. Zehentmeier S, Lim VY, Ma Y, et al. Dysregulated stem cell niches and altered lymphocyte recirculation cause B and T cell lymphopenia in WHIM syndrome. *Sci Immunol*. 2022;7(75):eabo3170.

66. Geier CB, Ellison M, Cruz R, et al. Disease Progression of WHIM Syndrome in an International Cohort of 66 Pediatric and Adult Patients. *J Clin Immunol*. 2022;42(8):1748-1765.

67. Kumar R, Milanesi S, Szpakowska M, et al. Reduced G protein signaling despite impaired internalization and β-arrestin recruitment in patients carrying a $CXCR4^{Leu317fsX3}$ mutation causing WHIM syndrome. *JCI Insight*. 2023;8(5):e145688.

68. Heusinkveld L, Majumdar S, Gao J-L, et al. WHIM Syndrome: from Pathogenesis Towards Personalized Medicine and Cure. *J Clin Immunol*. 2019;39(6):532-556.

69. Zmajkovicova K, Pawar S, Maier-Munsa S, et al. Genotype-phenotype correlations in WHIM syndrome: a systematic characterization of $CXCR4^{WHIM}$ variants. *Genes Immun*. 2022;23(6):196-204.

70. Badolato R, Alsina L, Azar A, et al. A phase 3 randomized trial of mavorixafor, a CXCR4 antagonist, for WHIM syndrome. *Blood*. 2024;144(1):35-45.

71. Lai AY, Watanabe A, O'Brien T, Kondo M. Pertussis toxin-sensitive G proteins regulate lymphoid lineage specification in multipotent hematopoietic progenitors. *Blood*. 2009;113(23):5757-64.

72. Messina-Graham S and Broxmeyer H. SDF-1/CXCL12 modulates mitochondrial respiration of immature blood cells in a bi-phasic manner. *Blood Cells Mol Dis*. 2016:58:13-8.

73. Biajoux V, Natt J, Freitas C, et al. Efficient Plasma Cell Differentiation and Trafficking Require Cxcr4 Desensitization. *Cell Rep.* 2016;17(1):193-205.

74. Alouche N, Bonaud A, Rondeau V, et al. Hematologic disorder-associated *Cxcr4* gain-of-function mutation leads to uncontrolled extrafollicular immune response. *Blood.* 2021; 137(22):3050-3063.

75. Six EM, Bonhomme D, Monteiro M, et al. A human postnatal lymphoid progenitor capable of circulating and seeding the thymus. *J Exp Med*. 2007;204(13): 3085–3093.

76. Thai L-H, Le Gallou S, Robbins A, et al. BAFF and CD4 + T cells are major survival factors for long-lived splenic plasma cells in a B-cell – depletion context. *Blood.* 2018;131(14):1545–1555.

77. Babicki S, Arndt D, Marcu A, et al. Heatmapper: web-enabled heat mapping for all. *Nucleic Acids Res.* 2016;44(W1):W147–53.

78. Dobin A, Davis CA, Schlesinger F, et al. STAR: ultrafast universal RNA-seq aligner. *Bioinformatics*. 2013;29(1):15-21.

79. Anders S, Pyl PT, Huber W. HTSeq-a python framework to work with high-throughput sequencing data. *Bioinformatics*. 2015;31(2):166-9.

80. Anders S, Huber W. Differential expression analysis for sequence count data. *Genome Biol*. 2010;11(10):R106.

81. Raudvere U, Kolberg L, Kuzmin I, et al. g:Profiler: a web server for functional enrichment analysis and conversions of gene lists. *Nucleic Acids Res.* 2019;47(W1):W191-W198.

82. Buenrostro JD, Giresi PG, Zaba LC, et al. Transposition of native chromatin for fast and sensitive epigenomic profiling of open chromatin, DNA-binding proteins and nucleosome position. *Nat Methods*. 2013;10(12):1213-8.

83. Langmead B, Trapnell C, Pop M, Salzberg SL. Ultrafast and memory-efficient alignment of short DNA sequences to the human genome. *Genome Biol*. 2009;10(3):R25.

84. Zhang Y, Liu T, Meyer CA, et al. Model-based analysis of ChIP-Seq (MACS). *Genome Biol*. 2008;9(9):R137.

85. Ramírez F, Ryan DP, Grüning B, et al. deepTools2: A next Generation Web Server for Deep-Sequencing Data Analysis. *Nucleic Acids Res*. 2016;44(W1):W160-5.

86. Shen L, Shao NY, Liu X, et al. diffReps: Detecting Differential Chromatin Modification Sites from ChIP-seq Data with Biological Replicates. *PLoS One*. 2013;8(6):e65598.

87. McLean CY, Bristor D, Hiller M, et al. GREAT improves functional interpretation of cis-regulatory regions. *Nat Biotechnol*. 2010;28(5):495-501.

88. Heinz S, Benner C, Spann N, et al. Simple combinations of lineage-determining transcription factors prime cis-regulatory elements required for macrophage and B cell identities. *Mol Cell*. 2010;38(4):576-89.

89. Bankhead P, Loughrey MB, Fernández JA, et al. QuPath: Open source software for digital pathology image analysis. *Sci Rep*. 2017;7(1):16878.

90. Schneider CA, Rasband WS, Eliceiri KW. NIH Image to ImageJ: 25 years of image analysis. *Nat Methods*. 2012;9(7):671-5.

91. Boots BN, Getis A. Point Pattern Analysis. *Newbury Park, CA: Sage*. 1988

92. Baddeley A, Rubak E, Turner R. Spatial Point Patterns: Methodology and Applications with R. *Chapman and Hall/CRC Press*. 2015.

Acknowledgements: We thank Drs. C. Doliger and S. Duchez (Flow Cytometry Core Facilities, Institut de Recherche Saint-Louis, Paris) for their technical assistance. The authors gratefully acknowledge the contribution of *Cxcl12*^{DsRed} knock-in reporter mice generated by S.J. Morrison (Ding and Morrison, 2013) and provided by Dr. L.G. Ng (Singapore Immunology Network, A*STAR, Singapore). We thank Dr. C. Jones and C. O'Brien (Princess Margaret Cancer Centre, Toronto, Canada) for editing the writing of our manuscript.

Funding: The study was supported by an ANR PRC grant (ANR-17-CE14-0019), an INCa grant (PRT-K 2017), the Association Saint Louis pour la Recherche sur les Leucémies and the FRM (Programme Equipe FRM 2022, EQU202203014627) to KB. V.R. was supported by the FRM, La Ligue Contre le Cancer and la Société Française d'Hématologie. M.K. was fellowship recipient from the French Ministry. Z.A-N. was fellowship recipient from the French Ministry and then supported by the FRM. J.L. was recipient from the People Programme (Marie Curie Actions) of the European Union's Seventh Framework Programme (FP7/2007-2013) under REA grant agreement n. PCOFUND-GA-2013-609102, through the PRESTIGE programme coordinated by Campus France, and from a ANR grant (ANR-17-CE14-0019). D.H.M and P.M.M. were supported by the Division of Intramural Research of the National Institute of Allergy and Infectious Diseases, National Institutes of Health.

Author contributions: V.R. designed and performed most of the experiments and contributed to manuscript writing; Ma.K., L.R., Z.A.N., V.G., A.B., J.L., Mé.K., C.M., B.S., S.L., C.F. and A.A. performed some of the experiments, analyzed data and reviewed the manuscript; M.D. and G.B. analyzed RNA-seq raw data; N.M., N.S., N.D., F.B. and M.A-L. contributed to data analyses and reviewed the manuscript; M.E. and S.J.C.M. helped with the study design, performed some of the experiments, contributed to data analyses and reviewed the manuscript; V.P. performed intravenous injections during in vivo experiments and reviewed the manuscript; D.S. performed artificial intelligence-based image analyses and reviewed the manuscript; C.L. performed and analyzed epigenetic studies and reviewed the manuscript; D.H.M. and P.M.M provided WS samples and clinical data and reviewed the manuscript; K.B. conceived, designed and supervised the study, contributed to data analyses, found funding for the study, and wrote the manuscript.

Competing Interests: The authors declare that they have no competing interests.

Data and materials availability: RNA-seq data that support the findings of this study have been deposited in the Gene Expression Omnibus repository with the accession code GSE182992. ATAC-seq data can be accessed on Gene Expression Omnibus repository under accession number GSE271225. All other data needed to evaluate the conclusions in the paper are present in the paper or the Supplementary Materials. The knock-in WHIM mice are available from INSERM under a material transfer agreement with the institution.

FIGURE LEGENDS

Fig. 1. The HSPC compartment is myeloid-skewed in the BM of WS mice and patients.

(A) Representative flow cytometric analyses show frequencies of MPP1, MPP2, MPP3, and MPP4 (gated on LSK and sorted on CD150, Flt3, CD48, and forward scatter (FSC)) as indicated, in the marrow fraction of WT, *Cxcr4*$^{+/1013}$ (+/1013), and *Cxcr4*$^{1013/1013}$ (1013/1013) mice. The bar graph shows the proportions of MPP1, MPP2, MPP3, and MPP4 in the marrow of WT and knockin mice. n= 8 independent experiments for a total of 22 WT, 22 +/1013 and 13 1013/1013 mice (MPP1) or n= 9 independent experiments for a total of 22 WT, 19 +/1013 and 13 1013/1013 mice (MPP2, MPP3, and MPP4). **(B)** Representative histograms show surface Cxcr4 abundance as determined by flow cytometry on MPP4 from the marrow fraction of WT and knockin mice. Background fluorescence is shown (isotype, gray histogram). Histograms are representative of n= 4 independent experiments for a total of 11 WT, 10 +/1013, and 8 1013/1013 mice. **(C)** Migration of WT and knockin MPP2 and MPP3 (MPP2-3) or MPP4 in response to Cxcl12 in the presence or absence of AMD3100 was assessed by flow cytometry. n= 3 independent experiments for a total of 9 WT, 6 +/1013 and 5 1013/1013 mice. **(D)** Representative histograms show the abundance of phosphorylated Akt (p-Akt) in MPP4 from WT and knockin mice stimulated with Cxcl12. Fluorescence in the absence of the p-Akt antibody (dashed line) or in absence of Cxcl12 stimulation (gray) are shown. The bar graphs show mean fluorescence intensity (MFI) for p-Akt determined by flow cytometry on MPP1, MPP2-3, and MPP4 from WT and knockin mice. n= 3 independent experiments for a total of 7 mice per group. **(E)** Absolute numbers of MPP1, MPP2, MPP3, and MPP4 in the marrow fraction of WT and knockin mice. n= 8 independent experiments for a total of 22 WT, 22 +/1013 and 13 1013/1013 mice (MPP1) or n= 9 independent experiments for a total of 22 WT, 19 +/1013 and 13 1013/1013 mice (MPP2-4). **(F)** Representative dot-plots obtained by flow cytometry show the frequencies of CD34^{+} cells in BM aspirates of n=4 healthy donors (HD) and n=2 WHIM Syndrome (WS) patients. **(G)** Pie chart representation of

the contribution of each HSPC subset to the total $CD34^+$ pool in representative HD and WS BM samples. **(H)** Representative dot-plots show the frequencies of CLPs ($CD34^+CD38^+CD45RA^+CD10^+$) among $CD34^+$ cells and the absolute numbers of CLPs in BM aspirates of HD and WS patients. **(I)** Representative histogram shows the detection of CXCR4 on the surface of $CD34^+$ cells from BM aspirates of HD and WS patients. Background fluorescence is shown (isotype, gray histogram). The graph shows the numbers of $CXCR4^+$ cells within $CD34^+$ cells from BM aspirates of HD and WS patients. Barplots indicate mean/SEM; horizontal lines correspond to median values. $^{\#}$ $P < 0.05$; $^{\#\#}$ $P < 0.005$; $^{\#\#\#}$ $P < 0.0005$ for Kruskal–Wallis tests; * $P < 0.05$; ** $P < 0.005$; *** $P < 0.0005$ for Dunn's test.

Fig. 2. CXCR4 desensitization is required for efficient generation and maintenance of the lymphoid-biased MPP4 pool. (A) Representative flow cytometric analyses comparing the frequencies of MPP3 and MPP4 (gated on LSK and sorted on CD150 and Flt3) 4 days after MPP1 from WT, +/1013, and 1013/1013 mice were cultured in the absence of AMD3100. Graphs show frequencies and absolute numbers of MPP3 and MPP4 in absence or presence of AMD3100. n= 6 independent experiments for a total of 10 WT, 7 +/1013, and 7 1013/1013 mice (no AMD3100) or 4 independent experiments for a total of 7 WT, 6 +/1013, and 3 1013/1013 mice (with AMD3100). **(B)** Heatmap of decreased ATAC-seq peaks in MPP1 from WT or knockin mice and gene ontology analysis with the genes associated with decreased ATAC-seq peaks in 1013/1013 vs WT MPP1. Data were generated using one replicate per group. Three mice of the same genotype were pooled to generate one replicate (3 mice for WT, 3 mice for +/1013, 3 mice for 1013/1013). **(C)** Highest enriched TF motifs in decreased ATAC-seq peaks in 1013/1013 vs WT MPP1. **(D)** Numbers of B cells after 14 days of coculture between WT or knockin MPP1 and OP9/IL-7 stromal cells. n= 3 independent experiments for a total of 3 mice per group. **(E)** Number of B cells ($B220^+CD11b^-$) after 7

days of coculture between MPP3 or MPP4 derived from WT or knockin MPP1 cultures and OP9/IL-7 stromal cells. n= 3 independent experiments for a total of 3 mice per group. **(F)** Heatmap of decreased ATAC-seq peaks in WT or knockin MPP4 and gene ontology analysis with the genes associated with decreased ATAC-seq peaks in 1013/1013 vs WT MPP4. Data were generated using two replicates per group. Three mice of the same genotype were pooled to generate the two replicates (3 mice for WT, 3 mice for +/1013, 3 mice for 1013/1013). **(G)** Highest enriched TF motifs in decreased ATAC-seq peaks in 1013/1013 vs WT MPP4. **(H)** Percentage of the indicated MPP subsets in G0 ($DAPI^{low}Ki\text{-}67^{-}$), G1 ($DAPI^{low}Ki\text{-}67^{+}$), S ($DAPI^{+}Ki\text{-}67^{+}$), and G2/M ($DAPI^{high}Ki\text{-}67^{+}$) phases. n= 5 independent experiments for a total of 15 WT, 15 +/1013, and 12 1013/1013 mice. Statistical significance compared to WT cells for each phase of the cell cycle is shown. $^{\#}$ $P < 0.05$; $^{\#\#}$ $P < 0.005$; for Kruskal–Wallis tests; * $P < 0.05$; ** $P < 0.005$ for Dunn's test; $^{£}$ $P < 0.05$; $^{££}$ $P < 0.005$; $^{£££}$ $P < 0.0005$ for Mann-Whitney's test.

Fig. 3. CXCR4 desensitization is required for MPP4 positioning near BM perivascular structures. (A) Schematic diagram for the generation of $CD45.2^{+}$->$CD45.1^{+}$ short-term (3 weeks) and long-term (16 weeks) BM chimeras. **(B)** Absolute numbers of donor-derived $CD45.2^{+}$ (WT, +/1013, or 1013/1013) MPP2, MPP3, and MPP4 recovered from the marrow of chimeras in $CD45.1^{+}$ WT recipients 3 weeks or 16 weeks after marrow transplantation. n= 3 independent experiments for a total of 5 WT, 8 +/1013, and 8 1013/1013 donor mice (3-week chimeras) or 4 independent experiments for a total of 17 WT, 19 +/1013, and 15 1013/1013 donor mice (16-week chimeras). **(C)** Schematic diagram for the generation of $CD45.1^{+}$ + $CD45.2^{+}$-> $CD45.1^{+}$/$CD45.2^{+}$competitive BM chimeras. **(D)** Relative contributions of $CD45.2^{+}$ and $CD45.1^{+}$ cells to donor-derived MPP2, MPP3, MPP4, and CLPs in the BM of $CD45.1^{+}$/$CD45.2^{+}$ WT recipient mice 3 weeks after competitive BM

transplantation. n=2 independent experiments for a total of 5 WT, 4 +/1013, and 4 1013/1013 donor mice. **(E)** Schematic diagram for the generation of $CD45.1^+$->$CD45.2^+$ short- and long-term BM chimeras. **(F)** Absolute numbers of donor $CD45.1^+$ WT MPP2, MPP3, and MPP4 recovered from the marrow of chimeras in $CD45.2^+$ (WT, +/1013, or 1013/1013) recipients 3 weeks or 16 weeks after marrow transplantation. n= 3 independent experiments for a total of 10 WT, 10 +/1013, and 5 1013/1013 recipient mice (3-week chimeras) or 4 independent experiments for a total of 12 WT, 11 +/1013, and 5 1013/1013 recipient mice (16-week chimeras). **(G)** Representative BM sections from WT and knockin mice stained to show laminin and nuclei (DAPI). MPP4 identified by RNA-scope and immunofluorescence staining (fig. S3, B and C) are indicated with yellow circles. Spatial distribution of centroids of MPP4 cells plot as yellow circles within points of DAPI detected cells (blue points). Scale bar, 800 μm. **(H)** Proportions of MPP4 (c-$Kit^+$$Sca\text{-}1^+$$Flt3^+$) detected in the BM sections of WT and knockin mice after imaging (fig. S3, B and C). n= 3 independent determinations for a total of 6 WT, 4 +/1013, and 4 1013/1013 mice. **(I)** Proportions of $Dsred^+$ cells within arteriolar cells ($Lam^+$$Sca\text{-}1^+$) in the BM sections of $Cxcr4^{+/+}Cxcl12^{Dsred}$, $Cxcr4^{+/1013}Cxcl12^{Dsred}$, and $Cxcr4^{1013/1013}Cxcl12^{Dsred}$ mice. n= 3 independent determinations for a total of 3 mice per group. **(J)** Spatial distance analysis between each MPP4 centroid and the centroid of the nearest arteriolar cell within representative BM sections from WT and knockin mice. Dots indicate individual MPP4 analyzed for one representative mouse per group with >140 cells analyzed. Quantifications are representative of 3 independent determinations per group. Mann–Whitney U test was used to assess statistical significance ($^{\text{££££}}$, $P < 0.0001$ between WT and 1013/1013 mice). **(K)** Representative histograms for intracellular antibody-based detection of phosphorylated STAT5 (p-STAT5) in sorted, untreated MPP4 from the marrow fraction of WT and knockin mice. Fluorescence in absence of the p-STAT5–specific antibody (dashed line) is shown. MFI values for p-STAT5 were determined by flow cytometry on

sorted MPP4 from the marrow fraction of WT and knockin mice. n= 3 independent experiments for a total of 3 WT, 2 +/1013 and 3 1013/1013 mice. # P < 0.05; ## P < 0.005; ### P < 0.0005 for Kruskal–Wallis tests; * P < 0.05; ** P < 0.005; *** P < 0.0005 for Dunn's test compared with WT, and § for Dunn's test comparing +/1013 and 1013/1013; ££££ P < 0.0001 for Mann-Whitney's test.

Fig. 4. CXCR4 desensitization is required to maintain the molecular identity of MPP4. **(A)** RNAseq data were generated from 3 x 10^3 MPP1-4 sorted from the marrow fraction of WT, +/1013, and 1013/1013 mice. **(B)** Volcano plots of differentially expressed genes in +/1013 vs. WT MPP4 and in 1013/1013 vs. WT MPP4. In each graph, the knockin is shown on the left and WT on the right. Genes highly differentially expressed (log2FC(knockin vs WT MPP4) > 2; -log10(adjusted p-value) > 2) are shown in red. Data were generated by RNA-seq from 2 (1013/1013 MPP4) or 3 (WT and +/1013 MPP4) independent experiments (9 mice each for WT and +/1013 MPP4, 6 mice for 1013/1013 MPP4). Three mice of the same genotype were pooled to generate one replicate. **(C)** Examples of biological processes for which 1013/1013 and WT MPP4 display differential gene expression signatures. Biological processes overrepresented in increased and decreased transcripts in 1013/1013 MPP4 compared to WT MPP4 were determined by Gene Ontology (GO) analyses.

Fig. 5. CXCR4 signaling termination is required to maintain the lymphoid potential in MPP4. (A) RNAseq-based heatmap showing normalized dye intensity for the expression of genes involved in lymphocyte differentiation (GO:0030098) in WT, +/1013, and 1013/1013 MPP4. Data were generated from 2 (1013/1013 MPP4) or 3 (WT and +/1013 MPP4) independent experiments (9 mice each for WT and +/1013 MPP4, 6 mice for 1013/1013 MPP4). Three mice of the same genotype have been pooled to generate one replicate. **(B)**

Biomark-based PCA of relative expression of selected genes involved in lympho-myeloid differentiation in MPP4. **(C)** The heatmap shows the relative quantification (RQ) for lymphoid transcripts normalized to *Actb* expression in each sample. The bar graph shows the RQ of the most decreased pro-lymphoid transcripts in MPP4. n = 4 WT, 3 +/1013, and 5 1013/1013 mice with samples from each mouse run in duplicate. **(D)** The heatmap shows the RQ for myeloid transcripts normalized to *Actb* expression in each sample. The bar graph shows the RQ of the most increased pro-GM transcripts in MPP4. n = 4 WT, 3 +/1013, and 5 1013/1013 mice with samples from each mouse run in duplicate. **(E)** Representative histograms for detection of Flt3 and Irf8 in MPP4. Fluorescence in absence of Irf8 antibody (dashed line) is shown. MFI values for surface Flt3 and proportions of $Irf8^{high}$ cells were determined by flow cytometry in MPP4. n = 6 independent experiments for a total of 11 WT, 18 +/1013, and 12 1013/1013 mice (Flt3) or n= 3 independent experiments for a total of 6 mice per group (Irf8). **(F)** Representative flow cytometric analyses comparing the frequencies of B cells ($B220^{+}CD11b^{-}$) between WT and knockin MPP4 co-cultures. Proportions of B cells after co-culture between MPP4 and OP9/IL-7 stromal cells in the presence or absence of AMD3100 were determined after 7 days. n = 3 independent experiments for a total of 4 WT, 3 +/1013, and 4 1013/1013 mice. **(G)** Representative flow cytometric analyses comparing the frequencies of $Lin^{-}Sca\text{-}1^{-}c\text{-}Kit^{+}$ [LK], $Lin^{-}Sca\text{-}1^{low}c\text{-}Kit^{low}$, $Gr1^{-}CD11b^{-}$ and $Gr1^{+}CD11b^{+}$ cells between WT and knockin MPP4 cultures at day 4 or day 7. Absolute numbers of GMPs were determined after 4 days of culture, whereas absolute numbers of $Gr1^{+}CD11b^{+}$ cells were assessed at day 7. Proportions of $Lin^{-}Sca\text{-}1^{low}c\text{-}Kit^{low}$ cells were determined after 4 days of culture. n= 4 independent experiments for a total of 8 WT, 8 +/1013, and 7 1013/1013 mice (day 4) or n= 3 independent experiments for a total of 7 WT, 7 +/1013 and 6 1013/1013 mice (day 7). **(H)** Proportions of MPP4 and $Flt3^{low}$ cells in WT and knockin MPP4 cultures after 4 days of differentiation in the presence or absence of AMD3100. n = 5 independent

experiments for a total of 10 WT, 11 +/1013, and 8 1013/1013 mice (no AMD3100) or n= 3 independent experiments for a total of 4 WT, 4 +/1013, and 3 1013/1013 mice (with AMD3100). **(I)** Expression of Flt3 determined by flow cytometry on MPP4 after 4 days of culture in the presence or absence of AMD3100. n= 3 independent experiments for a total of 4 WT, 4 +/1013, and 3 1013/1013 mice. **(J)** Proportions of donor $CD45.2^+$ myeloid or B cells recovered from the marrow of $CD45.1^+$ recipients 2 weeks after the transplantation. n= 2 independent experiments for a total of 6 WT, 5 +/1013, and 5 1013/1013 donor mice. **(K)** Absolute numbers of GMPs were determined after 4 days of WT MPP4 culture in the presence or absence of Cxcl12 and AMD3100 as indicated. Absolute numbers of $Gr1^+CD11b^+$ cells were assessed at day 7. n = 3 independent experiments for a total of 3 mice per group (day 4) or n= 5 independent experiments for a total of 9 mice per group (day 7). $^{\#}$ $P < 0.05$; $^{\#\#}$ $P < 0.005$ for Kruskal–Wallis tests; * $P < 0.05$; ** $P < 0.005$ for Dunn's test compared with WT, and § for Dunn's test comparing +/1013 and 1013/1013; $^{£}$ $P < 0.05$; $^{£££}$ $P < 0.0005$ for Mann-Whitney's test.

Fig. 6. Overactive OXPHOS-driven metabolism in $Cxcr4^{1013}$ knockin MPP4. (A) Representative histograms for intracellular detection of phosphorylated mTOR (p-mTOR) and phosphorylated S6 (p-S6) in MPP4 of the indicated genotypes stimulated with Cxcl12. Fluorescence of WT MPP4 in the absence of p-mTOR or p-S6 antibody (dashed line), in the absence of Cxcl12 stimulation (gray histogram) or in the presence of Cxcl12 and AMD3100 (black histogram) are shown. MFI values for p-mTOR and p-S6 were determined by flow cytometry. n=3 independent experiments for a total of 4 (with AMD3100) or 5 (no AMD3100) WT, 6 +/1013, and 6 1013/1013 mice. **(B)** OXPHOS and glycolytic contents measured by oxygen consumption rate (OCR) and extracellular acidification rate (ECAR), respectively, were determined in freshly sorted WT and 1013/1013 MPP4 by Seahorse Mito

Stress Test. n= 3 independent experiments for total of 9 WT, 9 +/1013, and 9 1013/1013 mice. Three mice of the same genotype were pooled for each independent experiment. Statistical significance compared with WT cells for each time point is shown. **(C)** Representative histograms and MFI values of TMRE and MTG staining in MPP4. n=3 independent experiments for a total of 10 WT, 10 +/1013, and 9 1013/1013 mice. **(D)** Representative images showing staining for TOMM20 and Hoechst 33342 in freshly isolated MPP4. Scale bar, 5 μm. n=3 independent determinations for a total of at least 50 cells analyzed per genotype. **(E)** MFI values of TOMM20 and number of mitochondrial fragments per WT MPP4 were determined using FIJI software. n=3 independent determinations for a total of at least 50 cells analyzed per condition (3 WT mice in total). **(F)** TMRE and MTG MFI values in WT MPP4 co-cultured with OP9/IL-7 cells. n= 3 independent experiments for a total of 3 mice per group. **(G)** Frequencies of $TMRE^{high/+}$ fraction A (FR. A) and $TMRE^{low/-}$ fraction B (FR. B) within WT and knockin MPP4. n= 3 independent experiments for a total of 8 WT, 8 +/1013, and 6 1013/1013 mice. **(H)** Absolute numbers of GMPs were determined after 4 days of fraction A or fraction B MPP4 culture, whereas absolute numbers of mature myeloid cells were assessed at day 7. n= 3 independent experiments for a total of 6 WT, 6 +/1013, and 5 1013/1013 mice (day 4) or n= 3 independent experiments for a total of 7 WT, 10 +/1013, and 7 1013/1013 mice (day 7). * for Dunn's test compared with WT cells, and £ for Mann-Whitney test comparing FR. A and FR. B. **(I)** Expression of pro-GM genes in single $TMRE^{low}$ (fraction B) MPP4 as determined by Biomark. Proportions of WT and 1013/1013 $TMRE^{low}$ MPP4 with detectable or undetectable expression of *Mpo* and *Irf8*. n= 2 independent experiments with > 50 cells per condition analyzed (2 mice of each genotype in total). **(J)** Proportions of donor $CD45.2^{+}$ (fraction A or B) myeloid or B cells recovered from the marrow of $CD45.1^{+}$ WT recipients 2 weeks after the transplantation. n= 2 independent experiments for a total of 3 mice per group. **(K)** Absolute numbers of mature myeloid cells in

WT or knockin MPP4 cultures in the presence or absence of Mito-q or CCCP were assessed at day 7. n= 3 independent experiments for a total of 3 mice per group. $^{\#}$ P < 0.05; $^{\#\#}$ P < 0.005; $^{\#\#\#}$ P < 0.0005 for Kruskal–Wallis tests; * P < 0.05; ** P < 0.005; **** P < 0.0001 for Dunn's test; $^{£}$ P < 0.05; $^{££}$ P < 0.005; $^{£££}$ P < 0.0005 for Mann-Whitney's test.

Fig. 7. Modulation of the Cxcr4-mTOR signaling axis normalizes the fate properties of Cxcr4^{1013} knockin MPP4. (A) Absolute numbers of GMPs were determined after 4 days of fraction B (TMRE^{low}) MPP4 culture in the presence or absence of AMD3100 or rapamycin, and absolute numbers of mature myeloid cells (Gr1^{+}CD11b^{+}) were assessed at day 7. n= 4 independent experiments for a total of 4 WT, 4 +/1013, and 3 1013/1013 mice (day 4) or n= 3 independent experiments for a total of 3 mice per group (day 7). * for Dunn's test comparing WT and 1013/1013, £ for Mann-Whitney test comparing PBS and AMD3100 or rapamycin. **(B)** Experimental procedure for in vivo AMD3100 treatment. At the end of the treatment, peripheral blood and BM were harvested 2 h after the last injection and analyzed by flow cytometry. **(C)** Absolute numbers of MPP4 were determined by flow cytometry in the marrow fraction of treated mice. n= 3 independent experiments for a total of 7 WT, 7 +/1013, and 5 1013/1013 mice (PBS condition) and a total of 10 WT, 10 +/1013, and 7 1013/1013 mice (AMD3100 condition). **(D)** Numbers of B cells (B220^{+}) and T cells (CD3^{+}) were determined in the peripheral blood of treated mice every 7 days. n= 3 independent experiments for a total of 7 WT, 7 +/1013, and 5 1013/1013 mice (PBS condition) and a total of 10 WT, 10 +/1013, and 7 1013/1013 mice (AMD3100 condition). Statistical significance compared to WT cells at day 21. **(E)** Representative histograms for TMRE staining in MPP4 from treated mice. The graph shows proportions of TMRE$^{low/-}$ fraction B among WT or knockin MPP4. n= 3 independent experiments for a total of 5 WT, 6 +/1013, and 5 1013/1013 mice (PBS condition) and a total of 9 WT, 9 +/1013, and 8 1013/1013 mice (AMD3100 condition). **(F)**

Representative histograms for intracellular detection of phospho-mTOR in $TMRE^{low}$ MPP4. Fluorescence in absence of phospho-mTOR antibody (dashed line), in absence of Cxcl12 stimulation (gray histogram) or presence of Cxcl12 and AMD3100 (black histogram) are shown. MFI values for phosphorylated mTOR (p-mTOR) were determined by flow cytometry. n= 3 independent experiments for a total of 3 WT, 3 +/1013, and 4 1013/1013 mice. **(G)** Representative flow cytometric analyses comparing the frequencies of B cells ($B220^{+}CD11b^{-}$) between 1013/1013 MPP4/OP9 cocultures at day 7 in the absence or presence of rapamycin. Graph shows the proportions of B cells after coculturing MPP4 with OP9/IL-7 stromal cells in the absence or presence of rapamycin after 7 days. n= 3 independent experiments for a total of 3 mice per group. **(H)** Absolute numbers of MPP4 determined by flow cytometry in the marrow fraction of treated mice 2 h after the last injection of rapamycin. n= 3 independent experiments for a total of 5 WT, 6 +/1013, and 3 1013/1013 mice (PBS condition) and a total of 9 WT, 10 +/1013, and 5 1013/1013 mice (rapamycin condition). **(I)** TMRE staining profiles in MPP4 from treated mice. n= 3 independent experiments for a total of 5 WT, 6 +/1013, and 3 1013/1013 mice (PBS condition) and a total of 9 WT, 10 +/1013, and 5 1013/1013 mice (rapamycin condition). **(J)** Numbers of B and T cells determined in the peripheral blood of treated mice every 7 days. n= 3 independent experiments for a total of 5 WT, 6 +/1013, and 3 1013/1013 mice (PBS condition) and a total of 9 WT, 10 +/1013, and 5 1013/1013 mice (Rapamycin condition). $^{\#}$ $P < 0.05$; $^{\#\#}$ $P < 0.005$; $^{\#\#\#}$ $P < 0.0005$ for Kruskal–Wallis tests; * $P < 0.05$; ** $P < 0.005$; for Dunn's test; $^{£}$ $P < 0.05$; $^{££}$ $P < 0.005$; $^{£££}$ $P < 0.0005$ for Mann-Whitney's test.

Fig. 8. **Model for CXCR4-mediated control of MPP4 fate.**

Collectively, our findings reveal an important role for the Cxcr4-mTOR signaling axis in regulating the fate of MPP4 and their mitochondrial machinery in mice. Cxcr4 desensitization

is required for the efficient generation of MPP4 from MPP1 and seems also necessary for their positioning near perivascular niches, allowing their access to external cues such as IL-7. Proper Cxcr4 signaling dampens MPP4 cycling and mTOR-dependent metabolic changes that promote myeloid differentiation, thereby allowing for the maintenance of high mitochondrial membrane potential ($TMRE^{high}$) and the lymphoid potential of MPP4. In the absence of Cxcr4 desensitization in WS mice, MPP1 displayed impaired capacity to differentiate into MPP4, and MPP4 localized at greater distances from arteriolar cells, likely resulting in suboptimal access to critical niche factors. Aberrant Cxcr4 signaling in MPP4 leads to enhanced mTOR signaling, overactive OXPHOS metabolism, and accumulation of damaged mitochondria with low membrane potential ($TMRE^{low}$), thereby promoting myeloid differentiation at the expense of the lymphoid lineage. Modulation of the Cxcr4-mTOR signaling axis using AMD3100 or rapamycin rescued the fate of MPP4 and their mitochondrial machinery in WS mice.

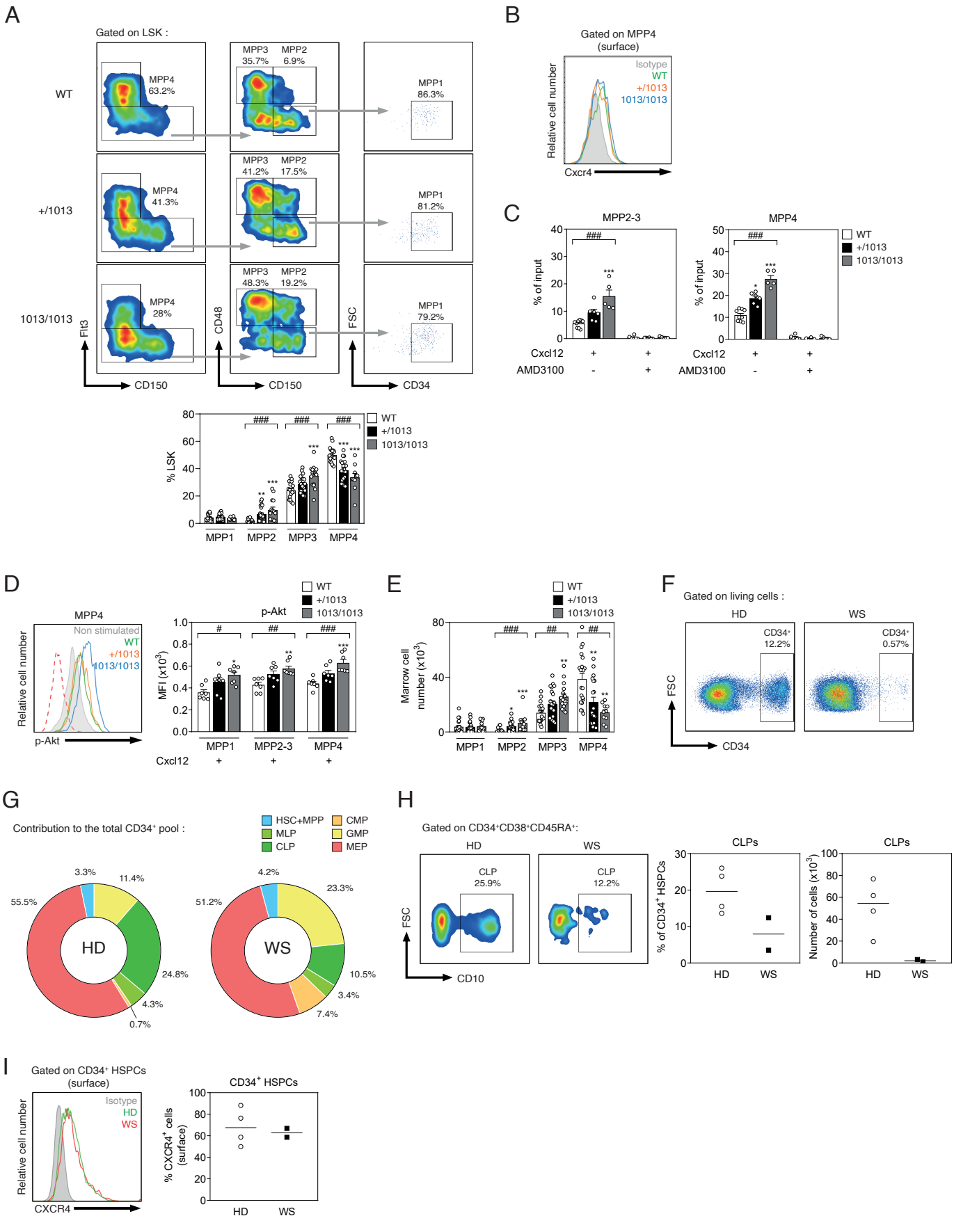
A
Gated on LSK :
WT
+/1013
1013/1013
MPP4 63.2%
MPP3 35.7%
MPP2 6.9%
MPP1 86.3%
MPP4 41.3%
MPP3 41.2%
MPP2 17.5%
MPP1 81.2%
MPP4 28%
MPP3 48.3%
MPP2 19.2%
MPP1 79.2%
Flt3
CD150
CD48
CD150
FSC
CD34
% LSK
MPP1
MPP2
MPP3
MPP4
WT
+/1013
1013/1013
B
Gated on MPP4 (surface)
Isotype
WT
+/1013
1013/1013
Relative cell number
Cxcr4
C
MPP2-3
MPP4
% of input
Cxcl12
AMD3100
WT
+/1013
1013/1013
D
MPP4
Non stimulated
WT
+/1013
1013/1013
Relative cell number
p-Akt
p-Akt
MFI (x10³)
MPP1
MPP2-3
MPP4
Cxcl12
E
Marrow cell number (x10³)
MPP1
MPP2
MPP3
MPP4
F
Gated on living cells :
HD
WS
CD34⁺ 12.2%
CD34⁺ 0.57%
FSC
CD34
G
Contribution to the total CD34⁺ pool :
HSC+MPP
MLP
CLP
CMP
GMP
MEP
HD
WS
3.3%
11.4%
55.5%
24.8%
4.3%
0.7%
4.2%
23.3%
51.2%
10.5%
3.4%
7.4%
H
Gated on CD34⁺CD38⁺CD45RA⁺:
HD
WS
CLP 25.9%
CLP 12.2%
FSC
CD10
CLPs
% of CD34⁺ HSPCs
Number of cells (x10³)
HD
WS
I
Gated on CD34⁺ HSPCs (surface)
Isotype
HD
WS
Relative cell number
CXCR4
CD34⁺ HSPCs
% CXCR4⁺ cells (surface)
HD
WS

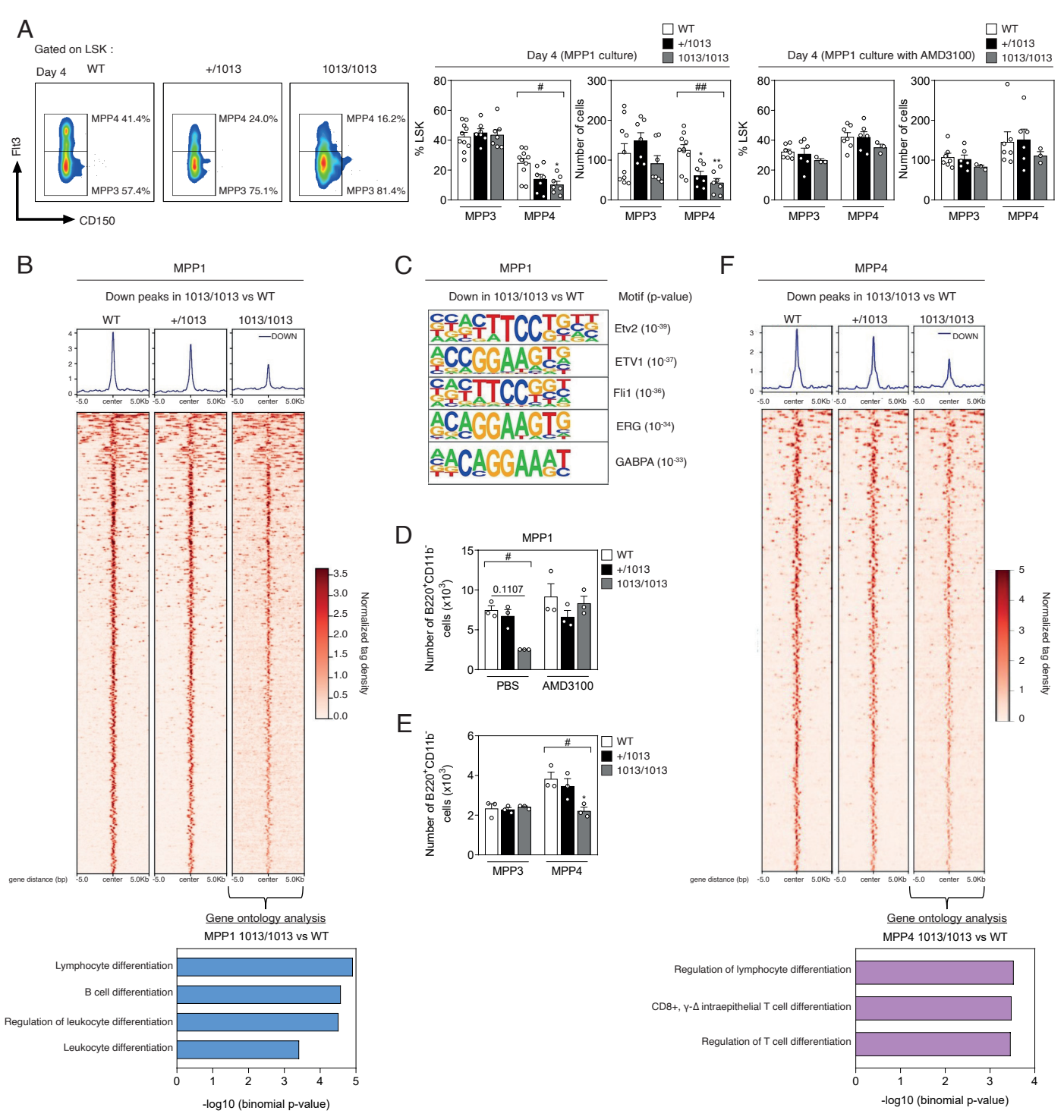
A
Gated on LSK :
Day 4
WT
+/1013
1013/1013
MPP4 41.4%
MPP3 57.4%
MPP4 24.0%
MPP3 75.1%
MPP4 16.2%
MPP3 81.4%
Flt3
CD150
Day 4 (MPP1 culture)
Day 4 (MPP1 culture with AMD3100)
WT
+/1013
1013/1013
% LSK
Number of cells
MPP3
MPP4
B
MPP1
Down peaks in 1013/1013 vs WT
WT
+/1013
1013/1013
DOWN
Normalized tag density
gene distance (bp)
Gene ontology analysis
MPP1 1013/1013 vs WT
Lymphocyte differentiation
B cell differentiation
Regulation of leukocyte differentiation
Leukocyte differentiation
-log10 (binomial p-value)
C
MPP1
Down in 1013/1013 vs WT
Motif (p-value)
Etv2 (10-39)
ETV1 (10-37)
Fli1 (10-36)
ERG (10-34)
GABPA (10-33)
D
MPP1
Number of B220+CD11b- cells (x10^3)
0.1107
PBS
AMD3100
E
Number of B220+CD11b- cells (x10^3)
MPP3
MPP4
F
MPP4
Down peaks in 1013/1013 vs WT
Gene ontology analysis
MPP4 1013/1013 vs WT
Regulation of lymphocyte differentiation
CD8+, γ-Δ intraepithelial T cell differentiation
Regulation of T cell differentiation
-log10 (binomial p-value)
G
MPP4
Down in 1013/1013 vs WT
Motif (p-value)
ERG (10-43)
Fli1 (10-36)
Etv2 (10-32)
EWS:FLI1 (10-31)
ETS1 (10-31)
H
% MPP1
% MPP2
% MPP3
% MPP4
G2/M
S
G1
G0

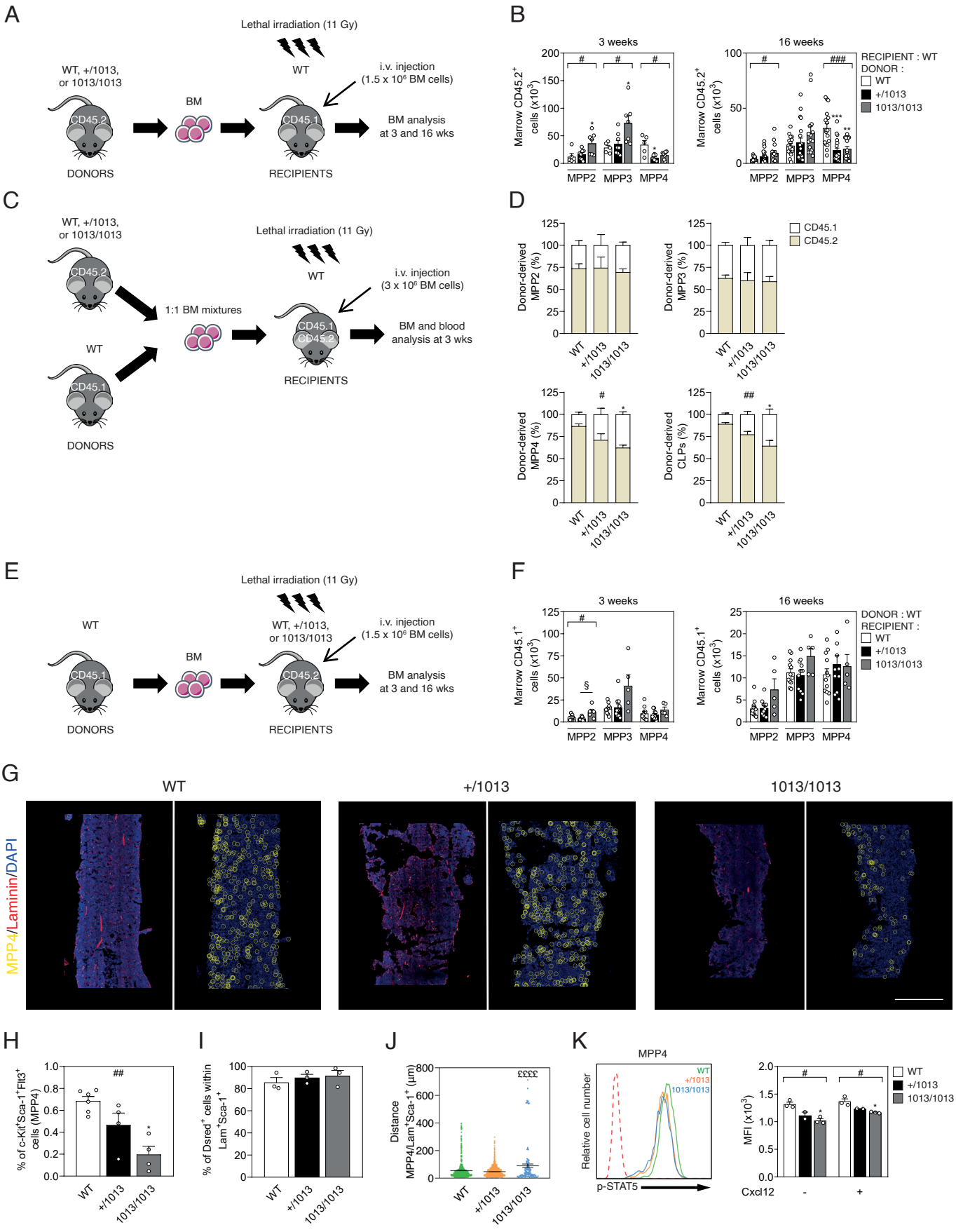
A
Lethal irradiation (11 Gy)
WT
WT, +/1013,
or 1013/1013
i.v. injection
(1.5 x 10⁶ BM cells)
BM
CD45.2
CD45.1
BM analysis
at 3 and 16 wks
DONORS
RECIPIENTS
B
3 weeks
16 weeks
Marrow CD45.2⁺ cells (x10³)
RECIPIENT : WT
DONOR :
WT
+/1013
1013/1013
MPP2
MPP3
MPP4
C
WT, +/1013,
or 1013/1013
Lethal irradiation (11 Gy)
WT
i.v. injection
(3 x 10⁶ BM cells)
1:1 BM mixtures
CD45.1
CD45.2
BM and blood
analysis at 3 wks
RECIPIENTS
DONORS
D
Donor-derived MPP2 (%)
Donor-derived MPP3 (%)
Donor-derived MPP4 (%)
Donor-derived CLPs (%)
CD45.1
CD45.2
WT
+/1013
1013/1013
E
Lethal irradiation (11 Gy)
WT
WT, +/1013,
or 1013/1013
i.v. injection
(1.5 x 10⁶ BM cells)
BM
BM analysis
at 3 and 16 wks
DONORS
RECIPIENTS
F
3 weeks
16 weeks
Marrow CD45.1⁺ cells (x10³)
DONOR : WT
RECIPIENT :
WT
+/1013
1013/1013
MPP2
MPP3
MPP4
G
WT
+/1013
1013/1013
MPP4/Laminin/DAPI
H
% of c-Kit⁺Sca-1⁺Flt3⁺ cells (MPP4)
WT
+/1013
1013/1013
I
% of Dsred⁺ cells within Lam⁺Sca-1⁺
J
Distance MPP4/Lam⁺Sca-1⁺ (μm)
K
MPP4
Relative cell number
WT
+/1013
1013/1013
p-STAT5
MFI (x10³)
Cxcl12

A

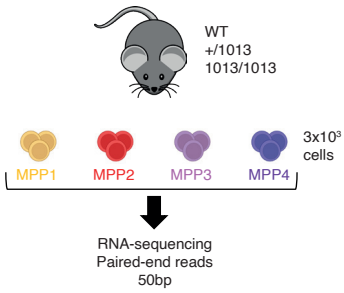
WT
+/1013
1013/1013
3x10³
cells
MPP1
MPP2
MPP3
MPP4
RNA-sequencing
Paired-end reads
50bp

B

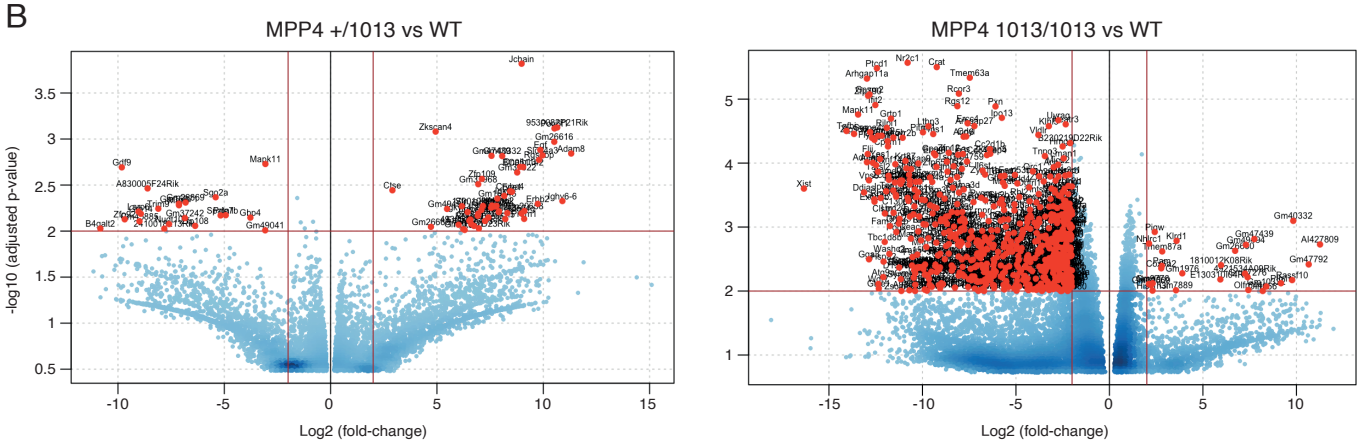
MPP4 +/1013 vs WT
MPP4 1013/1013 vs WT
-log10 (adjusted p-value)
Log2 (fold-change)
Jchain
Zkscan4
Magk11
Gdf9
Ctse
Gm40332
Gm47439
Gm47792
AI427809
Xist

C

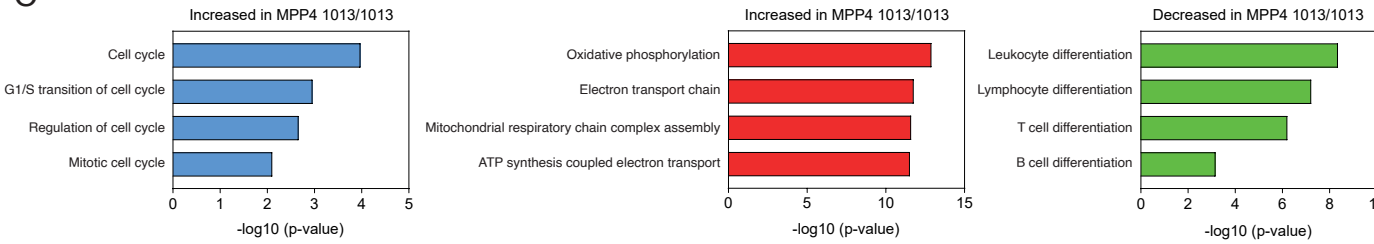
Increased in MPP4 1013/1013
Cell cycle
G1/S transition of cell cycle
Regulation of cell cycle
Mitotic cell cycle
-log10 (p-value)
Increased in MPP4 1013/1013
Oxidative phosphorylation
Electron transport chain
Mitochondrial respiratory chain complex assembly
ATP synthesis coupled electron transport
-log10 (p-value)
Decreased in MPP4 1013/1013
Leukocyte differentiation
Lymphocyte differentiation
T cell differentiation
B cell differentiation
-log10 (p-value)

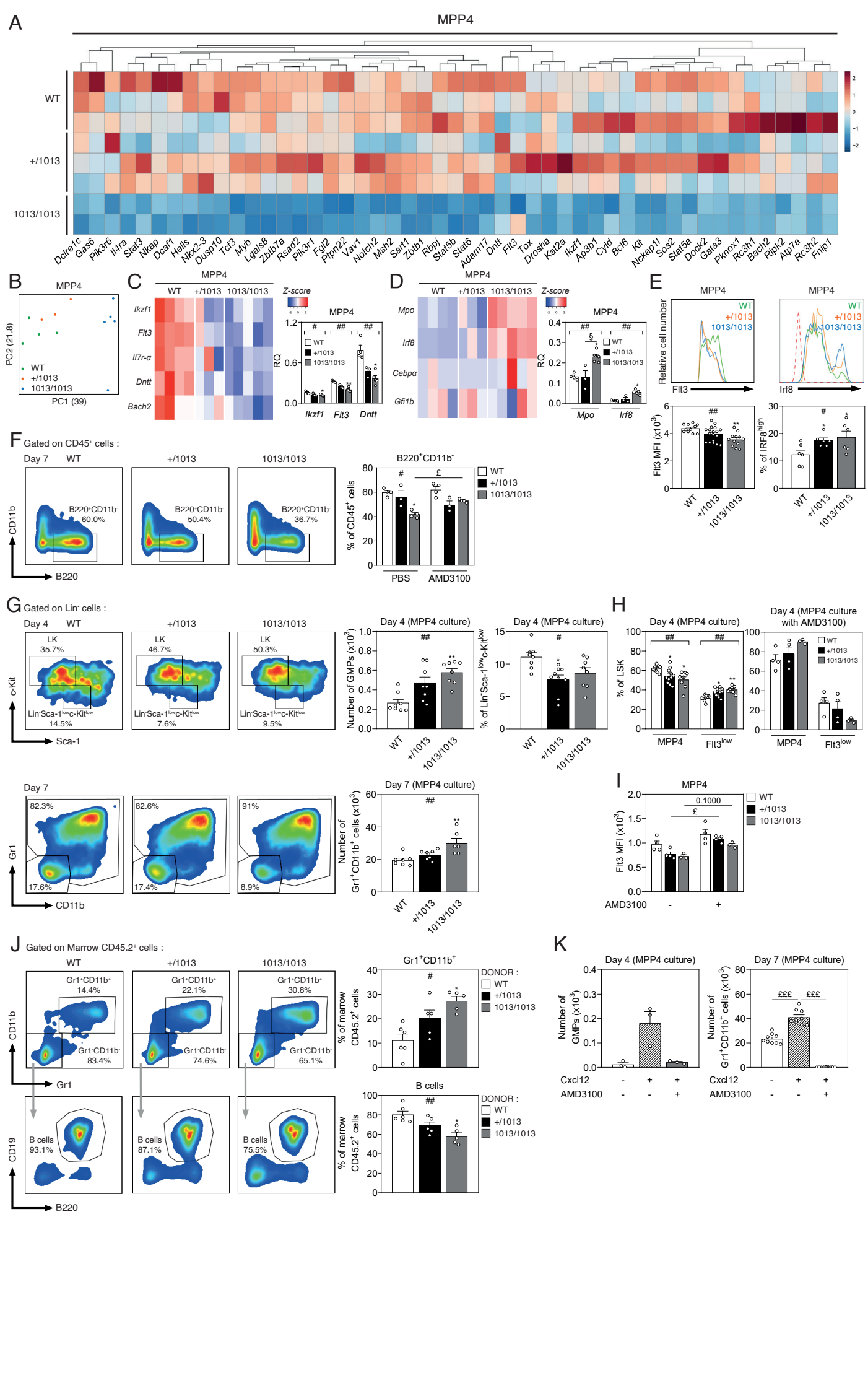
A
MPP4
WT
+/1013
1013/1013
Dclre1c Gas6 Plk3r6 Il4ra Stat3 Nkap Dcaf1 Hells Nkx2-3 Dusp10 Tcf3 Myb Lgals8 Zbtb7a Rsad2 Plk3r1 Fgl2 Ptpn22 Vav1 Notch2 Msh2 Sart1 Zbtb1 Rbpj Stat5b Stat6 Adam17 Dntt Flt3 Tox Drosha Kat2a Ikzf1 Ap3b1 Cyld Bcl6 Kit Nckap1l Sos2 Stat5a Dock2 Gata3 Pknox1 Rc3h1 Bach2 Ripk2 Atp7a Rc3h2 Fnip1
B
MPP4
PC2 (21.8)
PC1 (39)
WT
+/1013
1013/1013
C
MPP4
WT +/1013 1013/1013
Z-score
Ikzf1
Flt3
Il7r-α
Dntt
Bach2
MPP4
RQ
Ikzf1 Flt3 Dntt
D
MPP4
WT +/1013 1013/1013
Z-score
Mpo
Irf8
Cebpa
Gfi1b
MPP4
RQ
Mpo Irf8
E
MPP4
MPP4
WT
+/1013
1013/1013
Relative cell number
Flt3
Irf8
Flt3 MFI (x10³)
% of IRF8high
WT +/1013 1013/1013
F
Gated on CD45+ cells :
Day 7
WT
+/1013
1013/1013
B220+CD11b-
60.0%
50.4%
36.7%
CD11b
B220
B220+CD11b-
% of CD45+ cells
PBS
AMD3100
WT
+/1013
1013/1013
G
Gated on Lin- cells :
Day 4
WT
+/1013
1013/1013
LK
35.7%
46.7%
50.3%
Lin-Sca-1low c-Kitlow
14.5%
7.6%
9.5%
c-Kit
Sca-1
Day 4 (MPP4 culture)
Number of GMPs (x10³)
Day 4 (MPP4 culture)
% of Lin-Sca-1low c-Kitlow
WT +/1013 1013/1013
H
Day 4 (MPP4 culture)
% of LSK
MPP4
Flt3low
Day 4 (MPP4 culture with AMD3100)
WT
+/1013
1013/1013
MPP4
Flt3low
Day 7
82.3%
82.6%
91%
17.6%
17.4%
8.9%
Gr1
CD11b
Day 7 (MPP4 culture)
Number of Gr1+CD11b+ cells (x10³)
WT +/1013 1013/1013
I
MPP4
0.1000
Flt3 MFI (x10³)
WT
+/1013
1013/1013
AMD3100 - +
J
Gated on Marrow CD45.2+ cells :
WT
+/1013
1013/1013
Gr1+CD11b+
14.4%
22.1%
30.8%
Gr1-CD11b-
83.4%
74.6%
65.1%
CD11b
Gr1
B cells
93.1%
87.1%
75.5%
CD19
B220
Gr1+CD11b+
% of marrow CD45.2+ cells
DONOR :
WT
+/1013
1013/1013
B cells
% of marrow CD45.2+ cells
DONOR :
WT
+/1013
1013/1013
K
Day 4 (MPP4 culture)
Number of GMPs (x10³)
Cxcl12 - + +
AMD3100 - - +
Day 7 (MPP4 culture)
Number of Gr1+CD11b+ cells (x10³)
Cxcl12 - + +
AMD3100 - - +

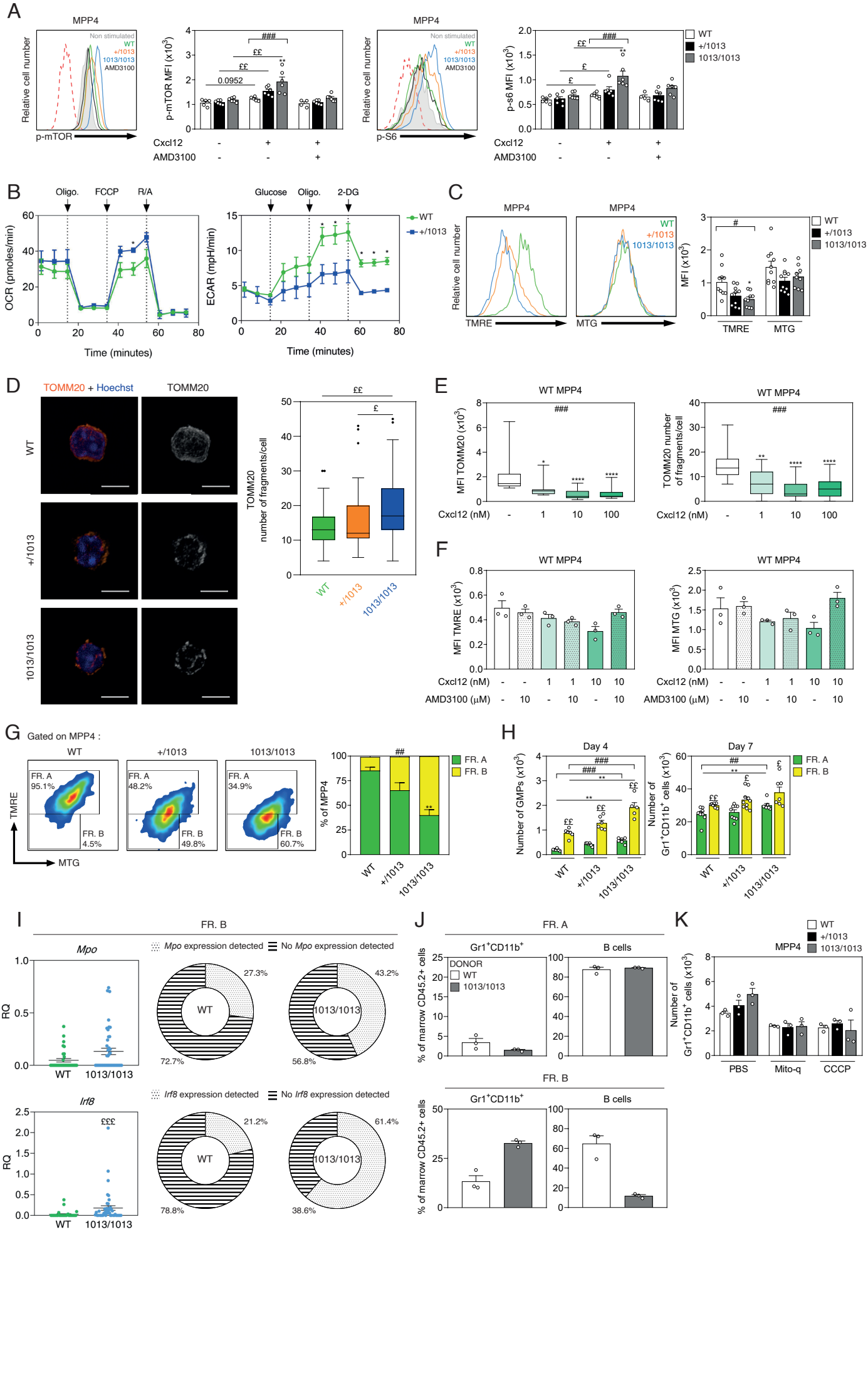
A
MPP4
Non stimulated
WT
+/1013
1013/1013
AMD3100
Relative cell number
p-mTOR
p-mTOR MFI (x10³)
0.0952
Cxcl12
AMD3100
MPP4
p-S6
p-s6 MFI (x10³)
WT
+/1013
1013/1013
B
Oligo.
FCCP
R/A
Glucose
Oligo.
2-DG
OCR (pmoles/min)
ECAR (mpH/min)
Time (minutes)
WT
+/1013
C
MPP4
TMRE
MTG
MFI (x10³)
D
TOMM20 + Hoechst
TOMM20
WT
+/1013
1013/1013
TOMM20 number of fragments/cell
E
WT MPP4
MFI TOMM20 (x10³)
TOMM20 number of fragments/cell
Cxcl12 (nM)
F
WT MPP4
MFI TMRE (x10³)
MFI MTG (x10³)
Cxcl12 (nM)
AMD3100 (μM)
G
Gated on MPP4 :
WT
+/1013
1013/1013
FR. A
FR. B
95.1%
4.5%
48.2%
49.8%
34.9%
60.7%
TMRE
MTG
% of MPP4
H
Day 4
Day 7
Number of GMPs (x10³)
Number of Gr1⁺CD11b⁺ cells (x10³)
I
FR. B
Mpo
Mpo expression detected
No Mpo expression detected
RQ
27.3%
72.7%
43.2%
56.8%
Irf8
Irf8 expression detected
No Irf8 expression detected
21.2%
78.8%
61.4%
38.6%
J
FR. A
Gr1⁺CD11b⁺
B cells
DONOR
WT
1013/1013
% of marrow CD45.2+ cells
FR. B
K
MPP4
Number of Gr1⁺CD11b⁺ cells (x10³)
PBS
Mito-q
CCCP

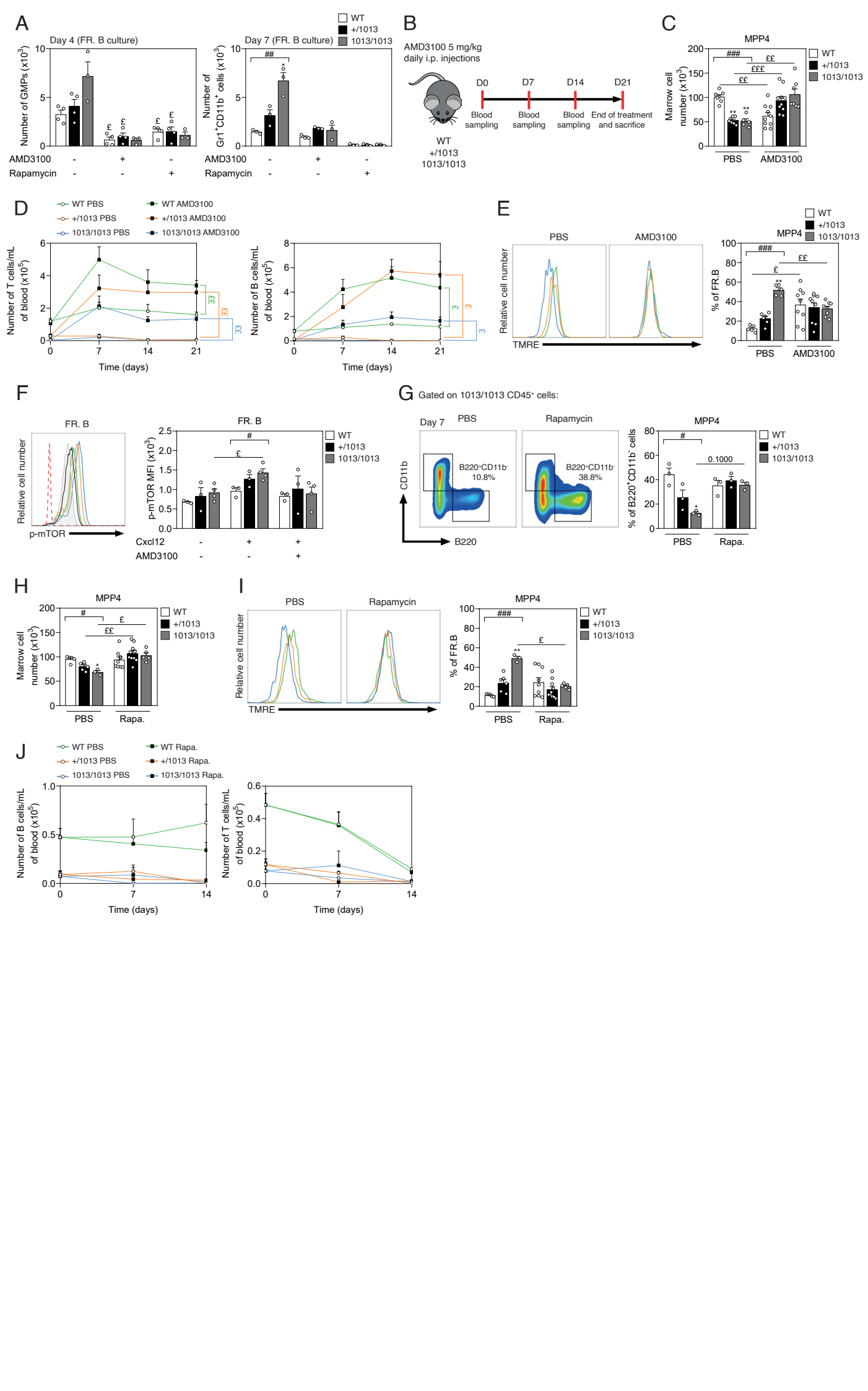
A
Day 4 (FR. B culture)
Day 7 (FR. B culture)
WT
+/1013
1013/1013
Number of GMPs (x10³)
Number of Gr1⁺CD11b⁺ cells (x10³)
AMD3100
Rapamycin
B
AMD3100 5 mg/kg
daily i.p. injections
WT
+/1013
1013/1013
D0
D7
D14
D21
Blood sampling
Blood sampling
Blood sampling
End of treatment and sacrifice
C
MPP4
Marrow cell number (x10³)
PBS
AMD3100
D
WT PBS
+/1013 PBS
1013/1013 PBS
WT AMD3100
+/1013 AMD3100
1013/1013 AMD3100
Number of T cells/mL of blood (x10⁵)
Number of B cells/mL of blood (x10⁵)
Time (days)
E
PBS
AMD3100
Relative cell number
TMRE
MPP4
% of FR.B
F
FR. B
Relative cell number
p-mTOR
p-mTOR MFI (x10³)
Cxcl12
AMD3100
G
Gated on 1013/1013 CD45⁺ cells:
Day 7
PBS
Rapamycin
CD11b
B220
B220⁺CD11b⁻ 10.8%
B220⁺CD11b⁻ 38.8%
% of B220⁺CD11b⁻ cells
0.1000
Rapa.
H
MPP4
Marrow cell number (x10³)
PBS
Rapa.
I
PBS
Rapamycin
Relative cell number
TMRE
MPP4
% of FR.B
J
WT PBS
+/1013 PBS
1013/1013 PBS
WT Rapa.
+/1013 Rapa.
1013/1013 Rapa.
Number of B cells/mL of blood (x10⁵)
Number of T cells/mL of blood (x10⁵)
Time (days)